Catalytic recycling of medical plastic wastes over $La_{0.6}Ca_{0.4}Co_{1−x}Fe_xO_{3−\delta}$ pre-catalysts for co-production of H_2 and high-value added carbon nanomaterials

Xiao Yu[1], Guoxing Chen[1*], Marc Widenmeyer[2], Isabel Kinski[1], Xingmin Liu[2], Ulrike Kunz[2] Dominique Schüpfer[1], Leopoldo Molina-Luna[2], Xin Tu[3], Gert Homm[1], Anke Weidenkaff[1,2]

[1]Fraunhofer Research Institution for Materials Recycling and Resource Strategies IWKS, Brentanostraße 2a, 63755 Alzenau, Germany

[2]Department of Materials and Earth Sciences, Technical University Darmstadt, Alarich-Weiss-Str. 2, 64287 Darmstadt, Germany

[3]Department of Electrical Engineering and Electronics, University of Liverpool, Liverpool L69 3GJ, UK

Abstract

In this work, waste medical masks collected from daily life usage were pyrolyzed and catalytically decomposed with perovskite-type $La_{0.6}Ca_{0.4}Co_{1−x}Fe_xO_{3−\delta}$ pre-catalysts for co-production of carbon nanomaterials and H_2. The influences of catalysis reaction temperature and Co/Fe ratio in the investigated pre-catalysts on the yields and selectivity of the gaseous products and carbon deposition were systematically studied. The physicochemical characteristics of the produced carbon nanomaterials were comprehensively characterized by the state-of-the-art techniques. $La_{0.6}Ca_{0.4}Co_{0.2}Fe_{0.8}O_{3−\delta}$ possessed the highest hydrogen and carbon nanomaterials yields at 850 °C among all the investigated pre-catalysts. Especially, this pre-catalyst showed an excellent performance during the 10 cycles of successive deconstruction of plastic wastes with the highest hydrogen yield of 34.33 mmol / $g_{plastic}$ at the 7th cycle. More importantly, carbon nanotubes generated had higher graphitic characteristics and fewer defects. The presented results demonstrated that the developed perovskite-type pre-catalyst is a promising candidate for the production of hydrogen and carbon nanotube composites for energy storge applications from medical waste plastics.

Email: guoxing.chen@iwks.fraunhofer.de
Keywords: perovskite, H_2 production, plastic recycling, carbon nanotube composites, pyrolysis-catalysis

1. Introduction

The global demand and consumption of plastic materials have significantly increased with the development of modern industry and population growth in the past few decades. It is reported that 367 million tons of plastics were produced in 2020, which was over 120 times than the value (3 million tons) in 1950 [1]. The COVID-19 pandemic further enhanced the consumption of medical plastic materials, which are used to produce single-use health protection products including facemasks and gloves.

The exploding consumption of plastics significantly increased the concerns of the post-customer wastes. For example, medical face masks are commonly made of non-degradable synthetic polymers such as polypropylene and polyethylene [2]. Typically disposal routes nowadays include thermal utilization (incineration) and landfill [3], which is environmentally unfriendly. Besides, about 10 % healthcare waste released from clinical and other health care facilities are containing infectious pathogens [2,4]. Their negative impacts on the environment, marine life, humans, and animals [5] have been proven by considerable recent studies. Therefore, more sustainable and efficient proper recycling strategies are highly needed to turn the medical plastic wastes into hazardous-free and value-added materials.

Chemical recycling approaches like pyrolysis, which can meet the disinfection conditions for coronavirus-contained objects reported by World Health Organization (WHO) and other literature [6], provides a cyclic economy approach to manage medical plastic wastes [7]. It can directly transform the plastic wastes into chemical products including H_2-rich gases, hydrocarbon fuels, and carbon nanomaterials [2,8–13]. Hydrogen as main gaseous product is a primary energy carrier, which is considered as an alternative choice for traditional fossil fuels in the future energy systems [14], especially for mobile applications. Comparing with gasoline and other liquid fuels, hydrogen's chemical energy density of 120 MJ/kg is at least three times higher [15–17]. Moreover, a hydrogen fuel cell electric vehicle converts energy at a higher rate (50–60%) than conventional cars that use fossil fuels and internal combustion engines whose maximum efficiencies are about 25% [17,18]. Carbon nanotubes (CNTs) which have been proven as one possible solid product from thermal disposal of plastic waste [19–21] are employed in various industrial sections especially in energy storage devices such as photovoltaic cells and lithium ion batteries [22–26] because of their remarkable physical and electrical properties. Several economic feasibility analyses have demonstrated that the scale of the plant is a crucial factor in determining the profitability of thermal pyrolysis technology [27]. Fivga et al. [28] conducted a sensitivity analysis and determined that for a plant with a capacity

of 100 kg/h of plastic waste, an external heating source is not necessary for the high temperature requirement of the process since the total thermal energy required by the pyrolysis reactor is more than three times smaller than the energy generated from burning the generated pyrolysis char and gases. Additionally, Osung et al. [29] pointed out that upscaling the pyrolysis plant to a feed rate of 50,000 tons/year resulted in a higher net present value (NPV) and greater economic competitiveness for the catalytic pyrolysis process compared to the pure thermal process. Moreover, catalytic pyrolysis also produced higher quality carbon and gas products, which is an added advantage. From an economic and sustainable perspective, pyrolysis presents a promising technique for converting a significant amount of mixed plastic waste that cannot be efficiently recovered through conventional mechanical recycling into hydrogen production and carbon capture and storage. This could play a critical role in the future energy infrastructure.

The introduction of a catalyst in the thermal pyrolysis process not only strengthens the gas production, but also serves as a critical factor for the formation of carbon nanotubes. Currently, the most applied catalysts are transition metal-based catalysts, in particular nickel- and iron-based catalysts [30–32]. Former is widely utilized in thermal treatment for hydrocarbon liquid and gas production [33], the other is often used to generate carbon nanotubes [34,35]. Moreover, a recent study illustrated that catalysts with a mixture of iron and nickel (bimetallic catalysts) convinced with a higher efficiency than single metal catalysts in the co-production of hydrogen and carbon nanotubes [36]. Apart from traditional metal-based catalysts, perovskite-type pre-catalysts have also been proven their excellent catalytic performance in methane decomposition [37] or reforming [38] for the production of hydrogen and carbon nanomaterials.

Catalysis temperature is another crucial parameter, having significant impacts on the yields of desired products. Several investigations have been conducted on pyrolysis with in-line catalytic deconstruction of plastics at temperatures ranging from 550 °C to 900 °C. Acomb et al. [20] and Jagodzińska et al. [39] discovered an intensification of filamentous carbon formation with increasing reaction temperature from 700 °C to 800 °C. However, further increasing of the temperature to 900 °C resulted in a decrease in non-condensable gases. Aside from the product yields, Liu et al. [40] and Jagodzińska et al. [39] observed an improvement on the quality (degree of carbonization) of CNTs when increasing the temperature up to 800 °C. Jia et al. discovered that higher catalytic temperatures of 900 °C caused a partial transition of CNTs into carbon nano-onions (CNOs) [41]. Therefore, the investigation in this study was extended to include a range of pre-catalyst bed temperatures, from 750 °C to 850 °C. Nevertheless, some barriers for the co-production of hydrogen and carbon nanotubes from plastic waste pyrolysis need to be addressed.

One issue for example is how to separate the formed CNTs from the catalysts for further use. Currently, most researches apply acids to separate the CNTs in the laboratory scale, it causes an obvious economic drawback when considering upscale the pyrolysis into an industrial scale. Pyrolysis of waste plastics employing perovskite-type materials to produce H_2 and composite materials may represent a potential solution to this problem since the metal oxide carbon composite materials products could be entirely applied without further separating process. Several studies have demonstrated that the generated metal oxide CNT composite materials could be utilized directly in energy-storage materials such as batteries [42–44] and solid oxide cells (SOCs) [45].

Therefore, investigations on the co-production of hydrogen and composite materials employing perovskite-type oxides are crucial. However, to the best of our knowledge, the utilization of perovskite-type pre-catalysts in the thermal deconstruction of (medical) plastic wastes has not been studied yet. In this work, we proposed a two-stage thermal process for upcycling wasted medical face masks with the introduction of a series of perovskite-type $La_{0.6}Ca_{0.4}Co_{1-x}Fe_xO_{3-\delta}$ ($x = 0.2, 0.5, 0.8$) pre-catalysts. The physicochemical properties of the pre-catalysts were characterized by state-of-the-art techniques. The influences of catalytic temperature and pre-catalyst composition on gas production and carbon species were investigated. Furthermore, the stability of the perovskite pre-catalysts and reproducibility was also studied through successive cyclic pyrolysis processes.

2. Experimental section

2.1 Pre-catalyst preparation

A reverse co-precipitation method was used to prepare the perovskite-type $La_{0.6}Ca_{0.4}Co_{1-x}Fe_xO_{3-\delta}$ ($x = 0.2, 0.5, 0.8$) pre-catalysts [46]. At a temperature of 60 °C, a weighed solution of metal nitrates ($La(NO_3)_3·6H_2O$ (Alfa Aesar, 99.9%), $Ca(NO_3)_2·4H_2O$ (SIGMA-ALDRICH, >99%), $Co(NO_3)_2·6H_2O$ (SIGMA-ALDRICH, >98%), and $Fe(NO_3)_3·9H_2O$ (SIGMA-ALDRICH, >98%)) was added to an ammonium carbonate solution slowly while vigorously stirred. To make a precipitate suspension, the pH was adjusted to 8.5–9 with ammonium carbonate (Alfa Aesar). The precipitates were aged at 60 °C for 1 hour while stirring, then filtered and washed multiple times with hot demineralized water to remove excess ions before drying at 110 °C for 12 hours. The dried material was crushed and calcined in air for 5 hours at 1050 °C to produce the final $La_{0.6}Ca_{0.4}Co_{1-x}Fe_xO_{3-\delta}$ ($x = 0.2, 0.5, 0.8$) pre-catalysts.

2.2 Characterization of materials

Powder X-ray diffraction (XRD) was used to determine the phase structures of the samples with a PANalytical empyrean X-ray diffractometer (Co-$K\alpha_1$). The diffraction patterns were recorded from 10° to 80° (2 theta) (scanning rate: 0.5 °/min). The surface texture information of the pre-catalysts is determined by N_2 adsorption at –196.15 °C using Brunauer–Emmett–Teller (BET) analysis (Micromeritics). The Raman spectra of the samples were measured using a micro-Raman spectrometer (Bruker) with a 532 nm laser as the excitation wavelength at 2 mW. Surface morphology of the samples was examined by a Zeiss-MERLIN scanning electron microscope (SEM) equipped with an OXFORD X-Max 80 X-ray detector for Energy-dispersive X-ray spectroscopy (EDXS). Temperature program oxidation (TPO) measurements were performed by using a NETZSCH STA 449F3. Around 30 mg sample was heated at a rate of 10 °C/min from room temperature up to 800 °C in an alumina crucible in air with a flow rate of 30 mL/min. The surface morphologies of the investigated perovskite pre-catalysts and produced carbon materials were examined by a JEM2100F (JEOL, Tokyo, Japan) transmission electron microscope (TEM) at 200 kV.

2.3 Experimental system

The experiments were performed in a dual-stage fixed bed system, and the schematic of the reactor system is displayed in Figure 1. It consists of a gas supply system, a reaction system, and a gaseous product condensing and collecting system. The reaction system is divided into two stages (two heating zones): the stage I for feedstock decomposition and the stage II for catalytic pyrolysis. The reaction temperatures of both stages can be controlled separately.

For each single experiment, 0.4 g of pre-catalyst (powder) was filled in a honeycomb ceramic holder loosely as shown in Figure 1, which was afterwards placed in the stage II of the reaction system. For the reference tests, only the honeycomb ceramic holder was used. Three different catalysis reaction temperatures of 750 °C, 800 °C, and 850 °C were studied in this work. Nitrogen with a flow rate of 120 mL/min was employed as the inert and carrier gas, which was controlled by a mass flow controller. Prior to the experiment, the entire system was firstly purged with nitrogen to ensure the inert condition. After reactor stage II with pre-catalysts reached pre-set temperature and kept stable, 1 g of used medical masks collected from the daily life usage was loaded in stage I and heated up to 500 °C with a heating rate of 15 °C/min and held for 15 min. Produced gaseous products from the system were introduced into the condenser system, and the non-condensable gas was collected with a 10 L gas sample bag for further analysis using Agilent gas-phase chromatograph (GC) equipped with a thermal conductivity

detector (TCD) and a flame ionization detector (FID). The N_2-flow was continued until the reactor system cooled down to room temperature, allowing all of the generated gases to be collected and providing an inert atmosphere for the produced solid products. Following that, solid residues, including spent pre-catalysts, were poured out of the honeycomb ceramic holder and saved for further analysis. To establish reliability, the reproducibility of the reaction system was investigated and experiments were repeated. Since C_3 and C_4 hydrocarbons were produced in very small quantities in this work (see Figure S1), which is also consistent with the previous reported studies [21,36]. Thus, the gas yields of these hydrocarbons were assumed to be zero in this work.
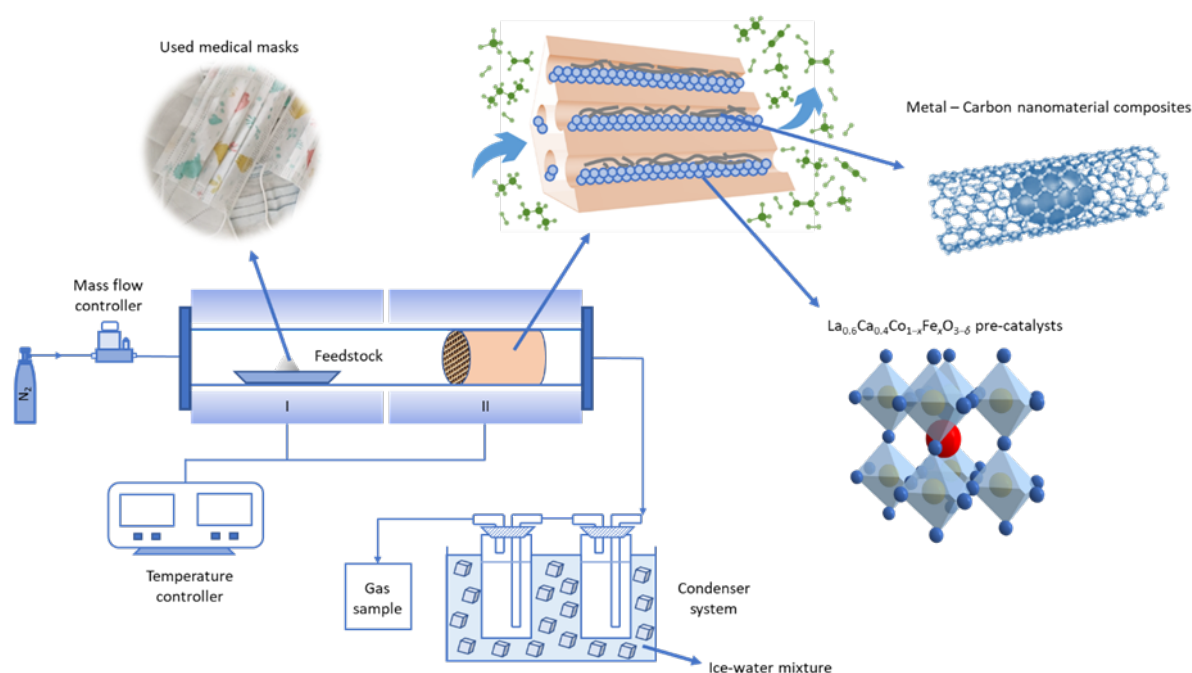
Figure 1. Schematic diagram of the pyrolysis process of plastic wastes system.

2.4 Definition of parameters

In this work, the mass of gaseous products was calculated based on the results from GC measurements. Each gas product can be determined by its relative volume percentage in the collected gas product mixture. The volume of each gas product can then be obtained. Based on that, the mass of each gas product can be calculated. The overall gas yield was calculated by the mass of generated gases divided by the total mass of wasted masks fed in the experiment (Equation 1). The solid (carbon) yield was determined by the mass difference between the spent and fresh pre-catalyst (Equation 2). The liquid yield was calculated by the mass change of the condenser system after each reaction (Equation 3).

$$\text{Gas yield (wt. \%)} = \frac{\text{mass of gas produced}}{\text{mass of medical mask}} \tag{1}$$

$$\text{Solid (carbon) yield (wt. \%)} = \frac{\text{mass of reacted pre−catalyst − mass of fresh pre−catalyst}}{\text{mass of medical mask}} \tag{2}$$

$$\text{Liquid yield (wt. \%)} =$$
$$\frac{\text{mass of condenser system after reaction − mass of condenser system before reaction}}{\text{mass of medical mask}} \tag{3}$$

Thereafter, the mass balance was estimated according to equation 4 for each test in this work in order to ensure the reliability of the experimental system.

$$\text{Mass balance (wt. \%)} = \text{Gas yield (wt. \%)} + \text{Solid yield (wt. \%)} + \text{Liquid yield (wt. \%)} \tag{4}$$

The H_2 yield was described as the millimoles of H_2 produced divided by the total weight of used plastic medical mask (Equation 5).

$$H_2 \text{ yield (mmol / } g_{plastic}) = \frac{\text{milimole of } H_2 \text{ produced}}{\text{mass of medical mask}} \tag{5}$$

3. Results and discussion

3.1 Characterization of fresh $La_{0.6}Ca_{0.4}Co_{1-x}Fe_xO_{3-\delta}$ pre-catalysts

Figure 2 shows the XRD patterns of $La_{0.6}Ca_{0.4}Co_{1-x}Fe_xO_{3-\delta}$ (x = 0.2, 0.5, 0.8). XRD patterns are displaying the characteristic reflections of the perovskite-type phase using a pseudo-cubic indexing. No impurities can be identified in the XRD patterns, which indicates that changing the Co/Fe ratio does not induce major changes in the crystal structure. As shown in Figure 2 (b) the reflection splitting suggests an orthorhombic structure [46,47]. However, the splitting vanishes with increasing Fe substitution content. In parallel, the position of the pseudo-cubic 110 reflection(s) shift(s) to a lower angle pointing to an expansion of the unit cell based on the larger ionic radius of iron (r(Fe^{3+}) = 0.645 Å) than cobalt (r(Co^{3+}) = 0.61 Å) [48] at the same oxidation state and coordination number. Figure 3 shows SEM images and EDXS elemental distribution of $La_{0.6}Ca_{0.4}Co_{1-x}Fe_xO_{3-\delta}$ pre-catalysts with different Co/Fe ratios. The morphologies of the different pre-catalysts are quite similar, which is also confirmed by the TEM images as shown in Figure S2. The EDXS analysis demonstrates that the elements including Ca, La, Co, O, and Fe, are uniformly distributed in the probed pre-catalyst surface for all the studied cases.
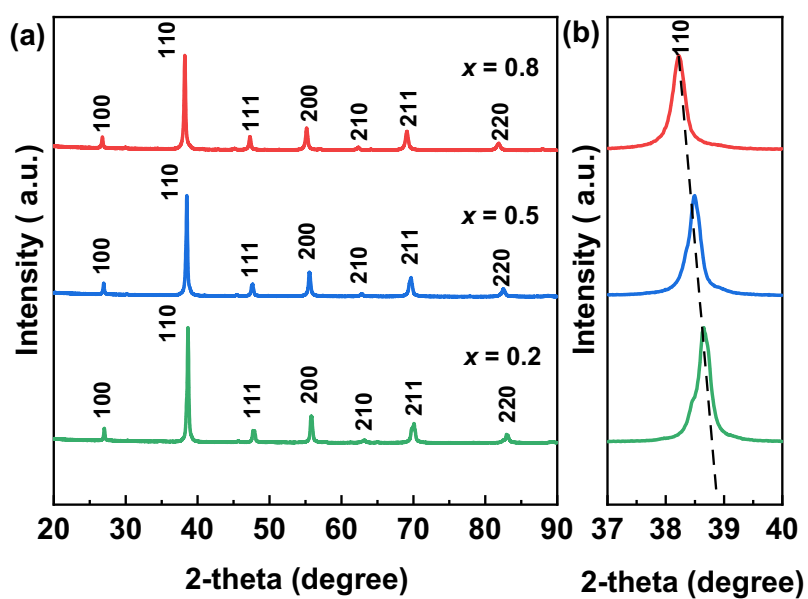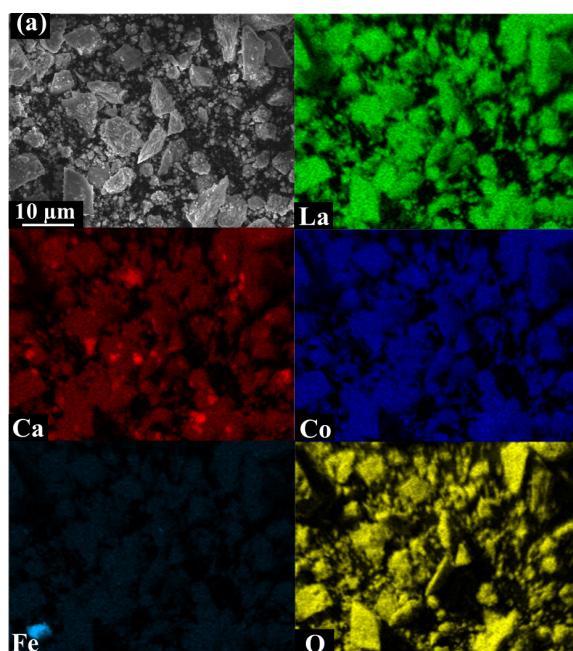
Figure 2. (a) XRD patterns of the $La_{0.6}Ca_{0.4}Co_{1-x}Fe_xO_{3-\delta}$ ($x = 0.2, 0.5, 0.8$) pre-catalysts; (b) close-up of the XRD patterns at $37° < 2\theta < 40°$.
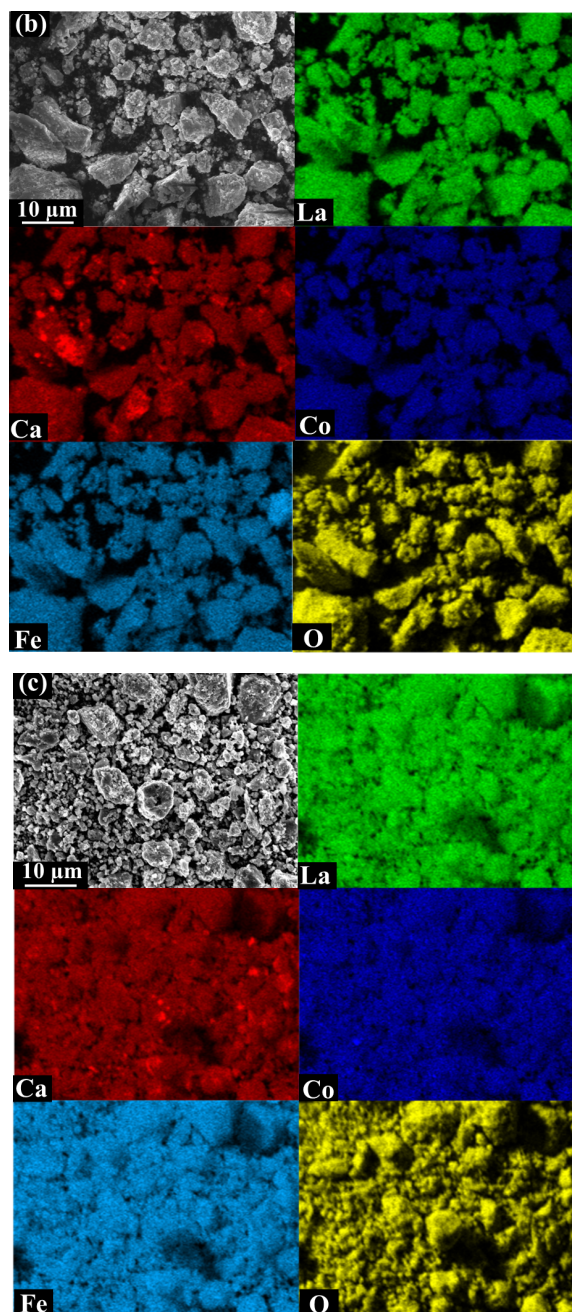
Figure 3. SEM images and EDXS elemental distribution of the fresh $La_{0.6}Ca_{0.4}Co_{1-x}Fe_xO_{3-\delta}$ ($x = 0.2$, 0.5, 0.8) pre-catalysts: (a) $x = 0.2$, (b) $x = 0.5$, and (c) $x = 0.8$.

3.2 Effect of reaction temperature on the product yield and gas composition

In this work, the thermal pyrolysis of used medical masks collected from daily life usage were investigated systematically at different reaction temperatures without and with perovskite-type $La_{0.6}Ca_{0.4}Co_{1-x}Fe_xO_{3-\delta}$ pre-catalysts in terms of product yields and selectivity. Table 1 displays the yields of products in different phases and the mass balance of each experiment. Generally, both gas and solid yields increased whereas liquid yields decreased as the reaction temperature

was raised from 750 °C to 850 °C at different catalytic conditions. When catalysts were introduced to the reaction system, there was a significant improvement on the solid yield upon the introduction of the pre-catalysts from 800°C to 850°C, which was consistent with the earlier findings [36,49]. Interestingly, at non-catalytic condition, the production of gas and solid were higher in our case compared to the previous research by Yao et al. [36]. This increase could be attributed to the employment of a honeycomb ceramic holder, which can transfer the heat better to the produced pyrolyzed gases, thereby increasing the conversion achieved by pure thermal pyrolysis. The mass balance was also studied for each experiment as shown in Table 1 to ensure the reliability of the reaction system. For some cases, the mass balance was relatively low, which can be attributed to the difficulties in collecting the liquid products since some of condensable vapors condensed on the wall of reactor. Figure 4 shows the productions of carbon and H_2 from thermal catalytic decomposition of plastics at different reaction temperatures. Under a non-catalytic condition, the H_2 yield showed an increase from 9.86 mmol / $g_{plastic}$ to 14.77 mmol / $g_{plastic}$ as rising the reaction temperature from 750 °C to 850 °C, but generally maintained at a relatively low level. Higher temperature promotes the decomposition of larger C_xH_y gas molecules into smaller ones and the tendency is in a good agreement with the reported results in literature [36]. Similarly, the carbon production illustrated in Figure 4 (a) was also enhanced by raising the reaction temperature in the absence of a pre-catalyst, improving from 95 mg/$g_{plastic}$ at 750 °C to 120 mg/$g_{plastic}$ at 850 °C, which indicated that carbon materials can be formed by pure thermal cracking.

Table 1. Results of pyrolysis and catalytic decomposition of medical plastic wastes at different reaction temperatures with $La_{0.6}Ca_{0.4}Co_{1-x}Fe_xO_{3-\delta}$ ($x = 0.2, 0.5, 0.8$) pre-catalysts.

Yield (wt. %)	Non-catalytic process			$La_{0.6}Ca_{0.4}Co_{0.8}Fe_{0.2}O_{3-\delta}$			$La_{0.6}Ca_{0.4}Co_{0.5}Fe_{0.5}O_{3-\delta}$			$La_{0.6}Ca_{0.4}Co_{0.2}Fe_{0.8}O_{3-\delta}$		
	750 °C	800 °C	850 °C	750 °C	800 °C	850 °C	750 °C	800 °C	850 °C	750 °C	800 °C	850 °C
Gas	41.5	55.5	55.1	40.1	44.6	47.9	33.3	42.5	47.4	33.5	39.6	45.1
Solid	9.5	11.0	12.0	10.5	11.0	18.5	11.5	20.8	22.3	11.0	21.5	24.5
Liquid	37.6	18.0	21.0	43.0	28.0	28.0	57.6	34.0	15.0	45.3	35.0	29.0
Mass balance	88.6	84.5	88.1	93.6	83.6	94.4	102.4	97.3	84.7	89.8	96.1	98.6

When the pre-catalysts were introduced to the reaction, there was a significant enhancement in the H_2 production. At a lower temperature of 750 °C, the yields of H_2 were similar over all

studied pre-catalysts with 16.94 mmol / $g_{plastic}$ for $La_{0.6}Ca_{0.4}Co_{0.8}Fe_{0.2}O_{3-\delta}$, 16.75 mmol / $g_{plastic}$ for $La_{0.6}Ca_{0.4}Co_{0.5}Fe_{0.5}O_{3-\delta}$, and 16.28 mmol / $g_{plastic}$ for $La_{0.6}Ca_{0.4}Co_{0.2}Fe_{0.8}O_{3-\delta}$. The generation of H_2 was steadily increased with increasing temperature for $La_{0.6}Ca_{0.4}Co_{0.8}Fe_{0.2}O_{3-\delta}$ and $La_{0.6}Ca_{0.4}Co_{0.5}Fe_{0.5}O_{3-\delta}$, reaching a maximum of 17.92 mmol / $g_{plastic}$ and 18.89 mmol / $g_{plastic}$, respectively. A further significant improvement of H_2 yield could be achieved by increasing the reaction temperature when $La_{0.6}Ca_{0.4}Co_{0.2}Fe_{0.8}O_{3-\delta}$ was employed, reaching a maximum of 24.92 mmol / $g_{plastic}$ at 850 °C, which was also the highest value among all the investigated reaction conditions.

Regarding the solid products from the catalytic process, the production of carbon was generally promoted by the presence of the pre-catalysts as well. In comparison to the non-catalytic case, carbon deposition was slightly improved over all the examined pre-catalysts at a lower temperature of 750 °C. The carbon deposition was considerably increased as the reaction temperature was raised. It is interesting to note that the carbon production was significantly enhanced with the rising substitution content of Fe in the studied $La_{0.6}Ca_{0.4}Co_{1-x}Fe_xO_{3-\delta}$ perovskite pre-catalysts, which can be attributed to the higher carbon solubility of Fe [50]. The maximum carbon deposition of 245 mg / $g_{plastic}$ was obtained in the presence of the $La_{0.6}Ca_{0.4}Co_{0.2}Fe_{0.8}O_{3-\delta}$ pre-catalyst at 850 °C. These findings indicate that Fe is more active in C_xH_y cracking, resulting in a higher hydrogen yield and carbon deposition, which is consistent with the previous findings [51,52]. However, complete substitution of Co by Fe in $La_{0.6}Ca_{0.4}Co_{1-x}Fe_xO_{3-\delta}$ ($x = 1$) resulted in a drop of both H_2 yield and carbon deposition at the same reaction condition at 850 °C (see Table S1). The slight increase in H_2 production with $La_{0.6}Ca_{0.4}Co_{0.5}Fe_{0.5}O_{3-\delta}$ in comparison to $La_{0.6}Ca_{0.4}Co_{0.8}Fe_{0.2}O_{3-\delta}$ as shown in Figure 4 can be explained in part by the smaller BET surface area of $La_{0.6}Ca_{0.4}Co_{0.5}Fe_{0.5}O_{3-\delta}$. Although the higher Fe content promotes the H_2 production (see Table S2).
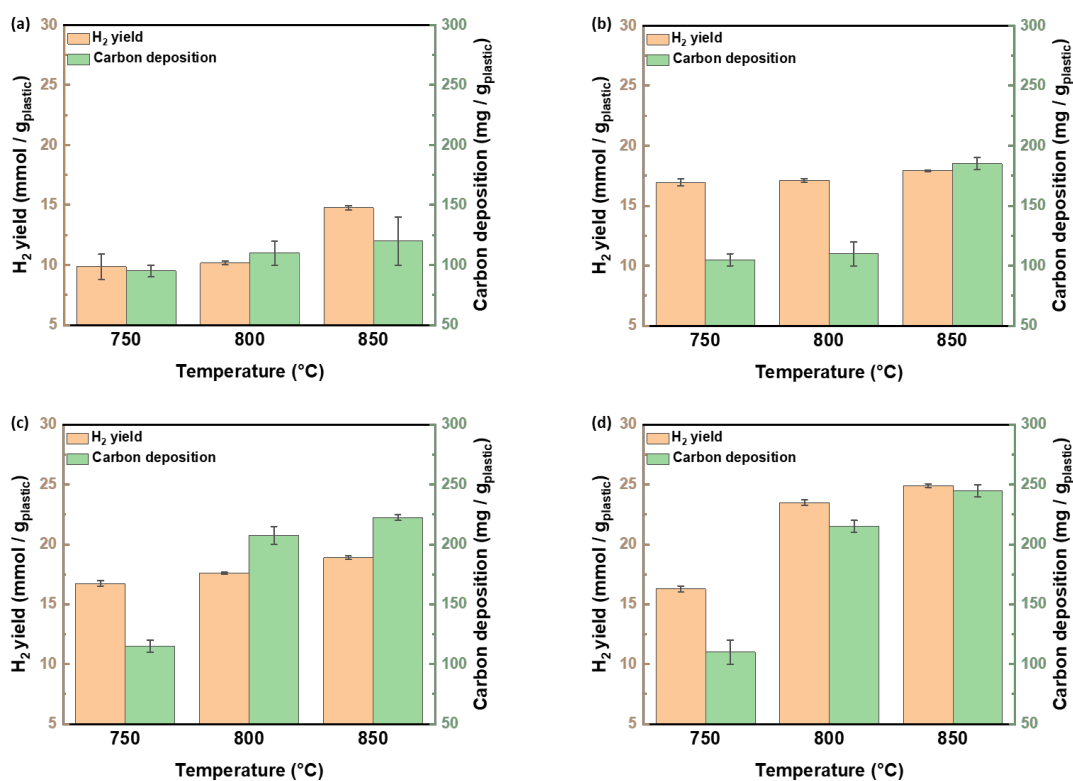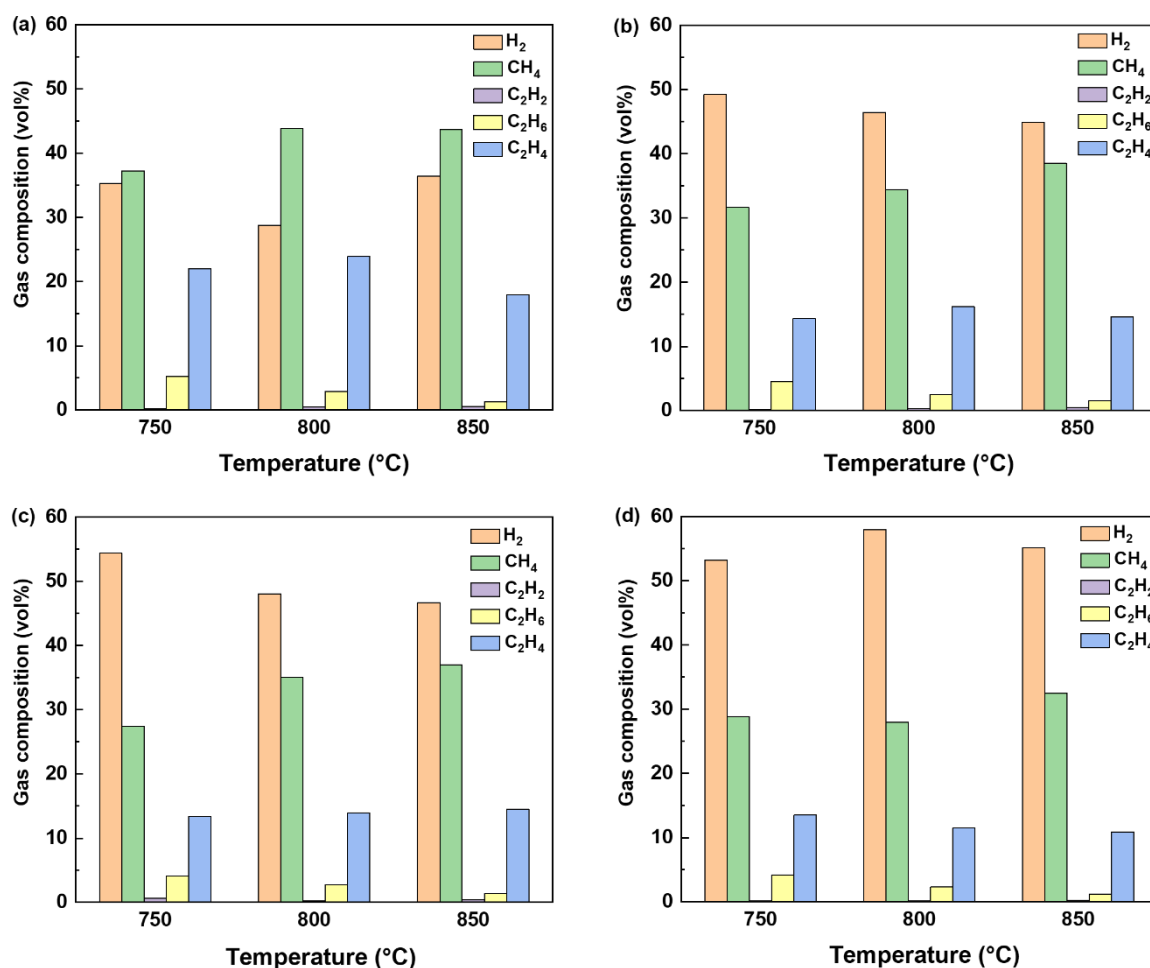
Figure 4. H_2 yield and carbon deposition at different reaction temperatures over (a) non-catalyst, (b) $La_{0.6}Ca_{0.4}Co_{0.8}Fe_{0.2}O_{3-\delta}$, (c) $La_{0.6}Ca_{0.4}Co_{0.5}Fe_{0.5}O_{3-\delta}$, and (d) $La_{0.6}Ca_{0.4}Co_{0.2}Fe_{0.8}O_{3-\delta}$.

Furthermore, the composition of produced gases was investigated and depicted in Figure 5. It can be observed from Figure 5(a), CH_4 and H_2 accounted for the majority of the gas products, taking 37.26 vol% and 35.28 vol%, respectively at 750 °C, then followed by C_2H_4, C_2H_6, and C_2H_2. Both CH_4 and H_2 had an increasing tendency when the temperature was raised to 850 °C, reaching 43.68 vol% and 36.49 vol%, respectively, whereas the volumetric content of C_2H_6 and C_2H_4 declined. These results agree well with the increased H_2 yield as shown in Figure 4 (a) that higher reaction temperature promotes the breakdown of larger C_xH_y gas molecules (C_2H_6 and C_2H_4) into smaller ones (H_2 and CH_4). In contrast to the non-catalytic process, H_2 had the highest concentration in the gaseous mixture for all the measurements in the presence of pre-catalysts at different reaction temperature as shown in Figure 5 (b)-(d). When raising the temperature from 750 °C to 850 °C, H_2 concentration in the gaseous mixture over both $La_{0.6}Ca_{0.4}Co_{0.8}Fe_{0.2}O_{3-\delta}$ and $La_{0.6}Ca_{0.4}Co_{0.5}Fe_{0.5}O_{3-\delta}$ showed small declines but remained at 44.9 vol% and 46.72 vol%, respectively, substantially greater than that from the non-catalytic thermal decomposition case (36.49 vol%). The highest H_2 proportion of 58 vol% again was obtained over $La_{0.6}Ca_{0.4}Co_{0.2}Fe_{0.8}O_{3-\delta}$ but with 800 °C at lower temperature. Higher reaction temperatures encouraged the breakup of C_xH_y gas molecules into smaller ones, which

corresponded to a drop in C_2H_6 and a rise in CH_4 in the presence of the pre-catalysts. Different starting weight ratios of medical masks to $La_{0.6}Ca_{0.4}Co_{0.2}Fe_{0.8}O_{3-\delta}$ pre-catalyst were also investigated at a reaction temperature of 850 °C (see Figure S3 and Figure S4). The results showed that the best H_2 and carbon materials yield was obtained with a weight ratio of 1:1, where the optimal weight ratio will allow the pre-catalyst to continue to work efficiently in the subsequent cycles of plastic waste degradation.

Figure 5. Gas composition at different reaction temperature over (a) non-catalyst, (b) $La_{0.6}Ca_{0.4}Co_{0.8}Fe_{0.2}O_{3-\delta}$, (c) $La_{0.6}Ca_{0.4}Co_{0.5}Fe_{0.5}O_{3-\delta}$, and (d) $La_{0.6}Ca_{0.4}Co_{0.2}Fe_{0.8}O_{3-\delta}$.

3.3 Carbon materials production over $La_{0.6}Ca_{0.4}Co_xFe_{1-x}O_{3-\delta}$ pre-catalysts

Figure 6, Figure 7, and Figure S5 present the SEM images of spent pre-catalysts with generated carbon materials at different catalytic conditions. In the low magnification SEM images (Figure 6), it can be observed that the surface of the studied perovskite-type pre-catalysts was completely covered with the produced carbon materials. Very crowded and dense material of

filamentous carbon can be observed for all examined pre-catalysts at the reaction temperatures of 750 °C and 800 °C. When further increasing the temperature to 850 °C, quite a lot of flocculation occurred and entangled filamentous carbon can be found, illustrating the formation of carbon materials with a higher density, which is consistent with the promoted carbon yield at higher temperature. The high magnification SEM images exhibited various shapes of the generated carbon materials such as silk-like (Figure 7 (b)), chain-like (Figure 7(c)), and spiral (Figure 7(f)). However, there is no clear evidence of a link showing the relationship between the morphology of carbon products and catalysis conditions. In order to have a more thorough examination of the structure of these filamentous carbons, TEM measurements have been employed. As noted from Figure 8, both carbon nanofibers and a multi-walled structure of the generated carbon nanotube composites can be observed. The carbon materials created in this work at 850 °C always displayed a bamboo-like structure, which is interestingly consistent with our earlier reported results regardless of the pre-catalyst composition [12]. Detailed analysis of temperature-programmed oxidation and Raman spectroscopy results in the subsequent section confirm that the carbon materials produced are primarily composed of carbon nanotubes with an outer diameter of approximately 50 nm. The mechanism of carbon nanotubes growth is complex and can vary depending on pre-catalysts, feedstocks, and reaction conditions. According to the literature [53], the formation of carbon nanotubes followed a three-step "particle-wire-tube" evolution mechanism: i) capturing of carbon species and the formation of nanoparticles; ii) self-assembling of nanoparticles to nanowires (particle-to-wire assembly); iii) transformation of nanowire to nanotubes. Figure 9 and Figure S6 show the TEM images with corresponding EDXS spectra of the carbon materials produced using different pre-catalysts at 850 C°. The dark spots (such as spots 3 , 4, and 6) in the images represent the metallic catalyst clusters where the nanocarbons grow, which is confirmed by the EDXS spectra (Figure S6). These findings suggest that the active sites for capturing carbon species and the formation of nanoparticles are Co and Fe produced in situ from the used pre-catalysts. The appreciable solubility of carbon in Fe and Co species is expected to result in carbon filament growth and metal encapsulation, as illustrated in Figure 9 (spots 1, 2, and 10).
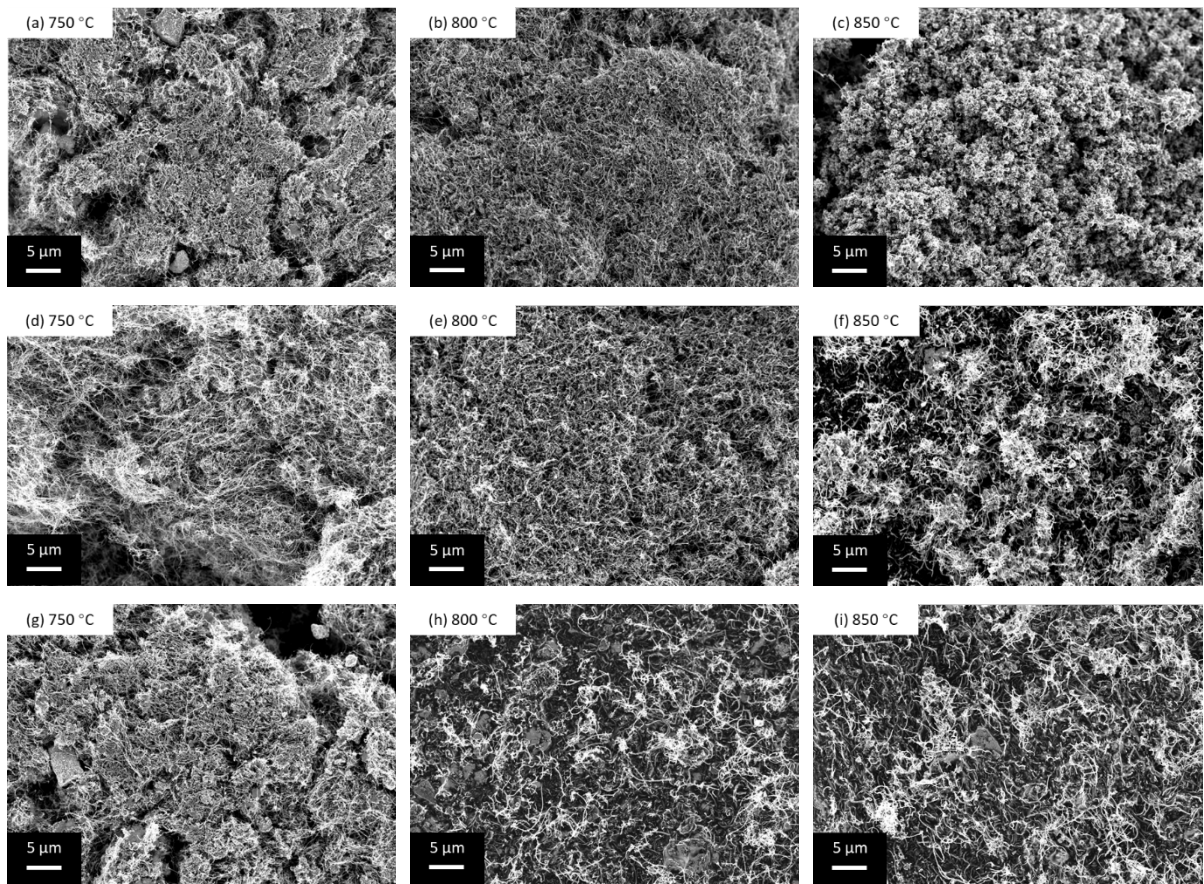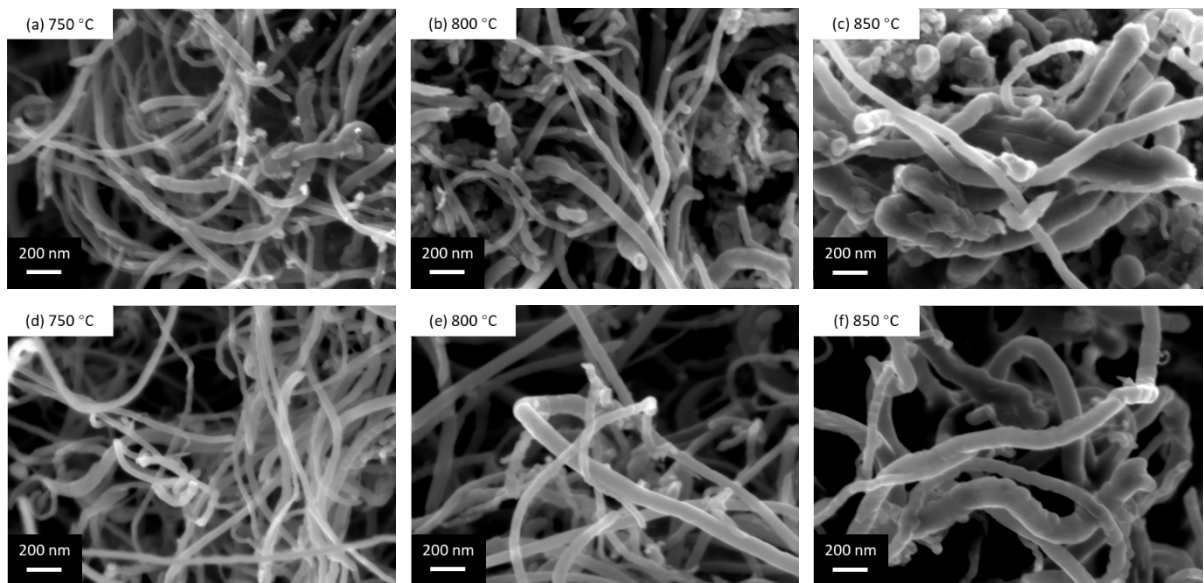
Figure. 6 Low magnification SEM images of the carbon materials synthesized with $La_{0.6}Ca_{0.4}Co_{1-x}Fe_xO_{3-\delta}$ (x = 0.2, 0.5, 0.8) pre-catalysts at different reaction temperatures (750 °C, 800 °C, and 850 °C): (a,b,c) x = 0.2, (d,e,f) x = 0.5, and (g,h,i) x = 0.8.
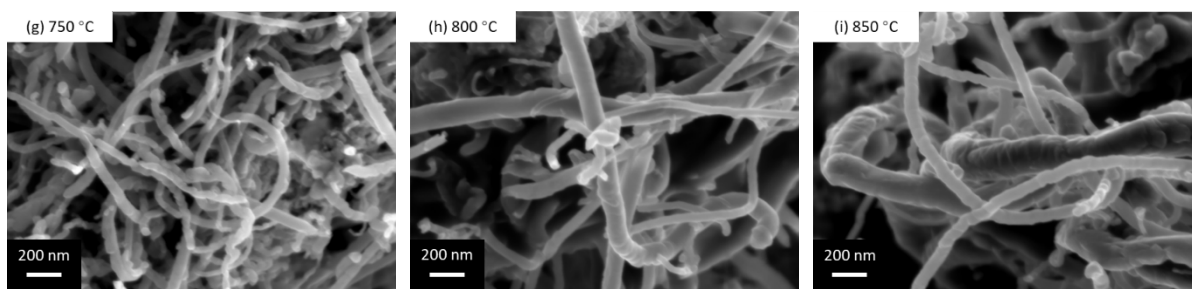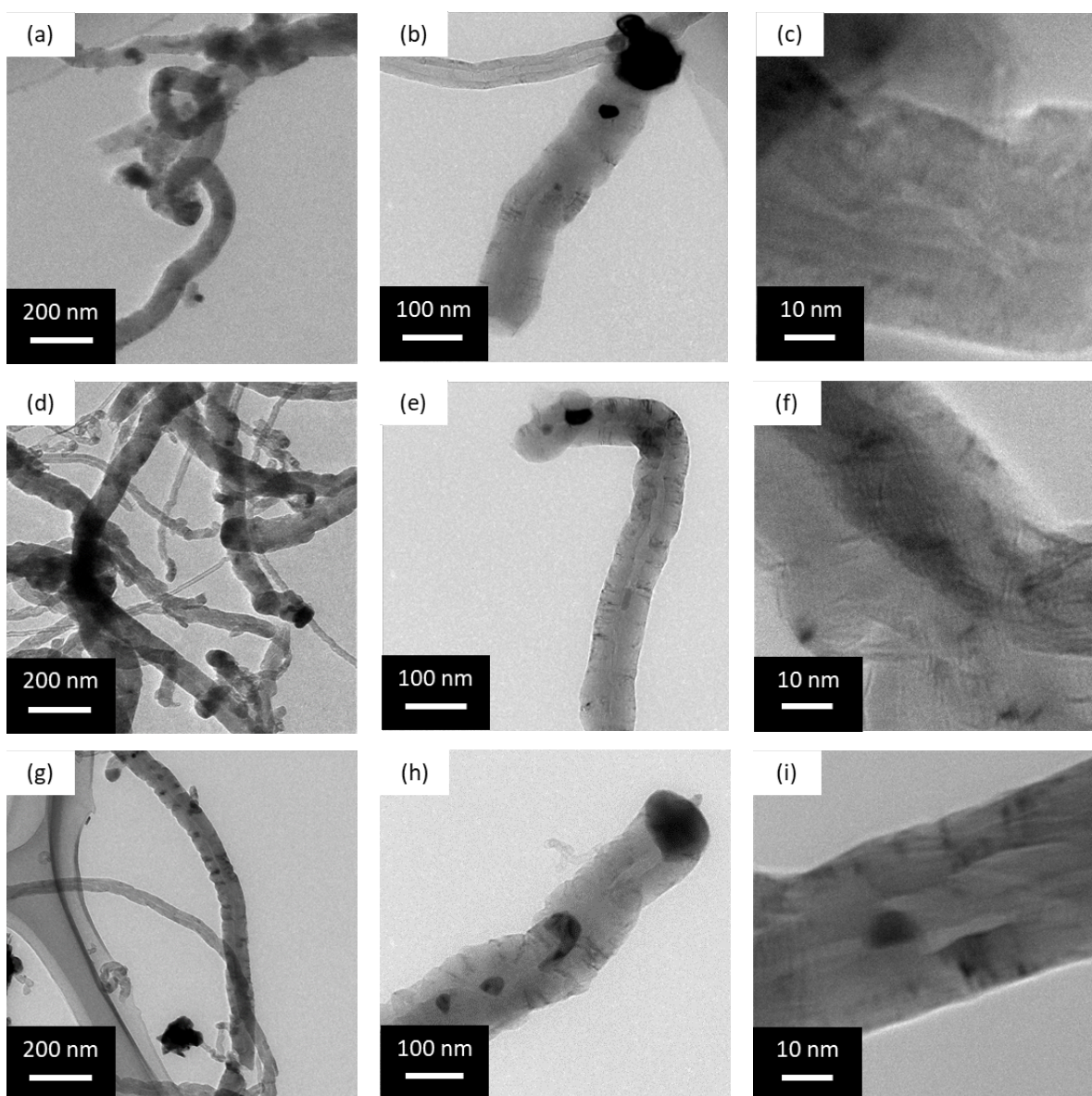
Figure. 7 High magnification SEM images of the carbon materials synthesized with $La_{0.6}Ca_{0.4}Co_{1-x}Fe_xO_{3-\delta}$ (x = 0.2, 0.5, 0.8) pre-catalysts at different reaction temperatures (750 °C, 800 °C, and 850 °C): (a,b,c) x = 0.2, (d,e,f) x = 0.5, and (g,h,i) x = 0.8.
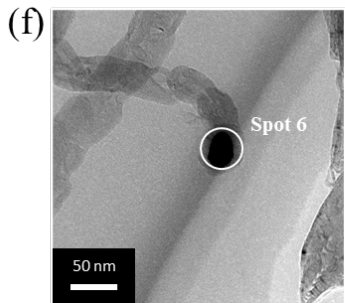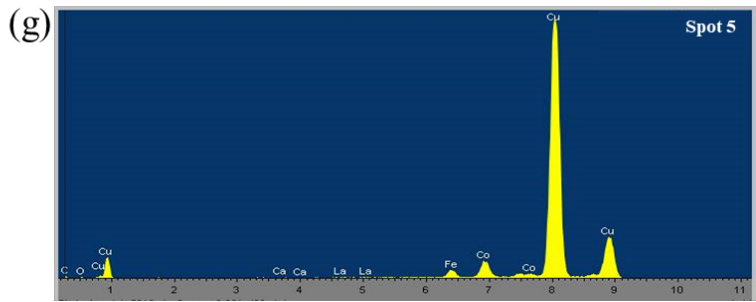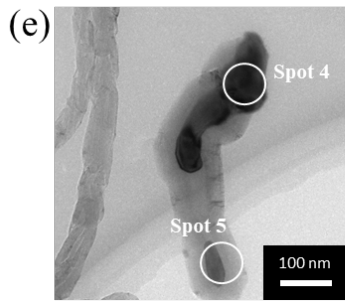

Figure 8. TEM images of the carbon materials produced using $La_{0.6}Ca_{0.4}Co_{1-x}Fe_xO_{3-\delta}$ (x = 0.2, 0.5, 0.8) pre-catalysts at a reaction temperature of 850 °C: (a,b,c) x = 0.2, (d,e,f) x = 0.5, and (g,h,i) x = 0.8.

(a)

Spot 1

100 nm

(b)

Spot 2

Spot 3

100 nm

(c)
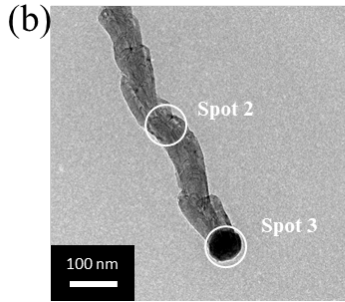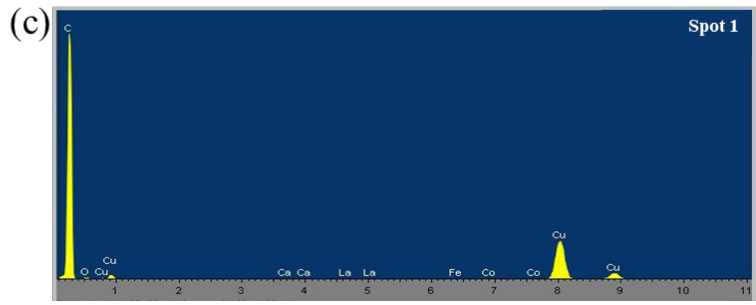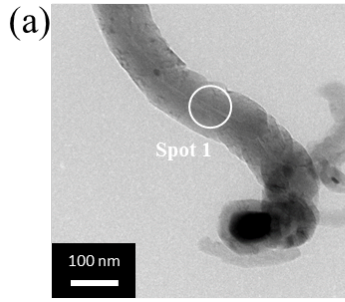
Spot 1

(d)

At%	C	O	Ca	Fe	Co	La
Spot 1	99.7	0.2	0.0	0.0	0.0	0.0
Spot 2	99.7	0.3	0.0	0.0	0.0	0.0
Spot 3	67.1	5.3	0.1	13.1	14.1	0.2

(e)

Spot 4

Spot 5

100 nm

(f)

Spot 6

50 nm

(g)

Spot 5

(h)

| At%	C	O	Ca	Fe	Co	La
Spot 4	2.7	0.7	0.1	27.2	69.4	0.0
Spot 5	15.6	5.6	0.0	23.8	54.9	0.0
Spot 6	30.7	6.0	0.3	34.9	27.8	0.4
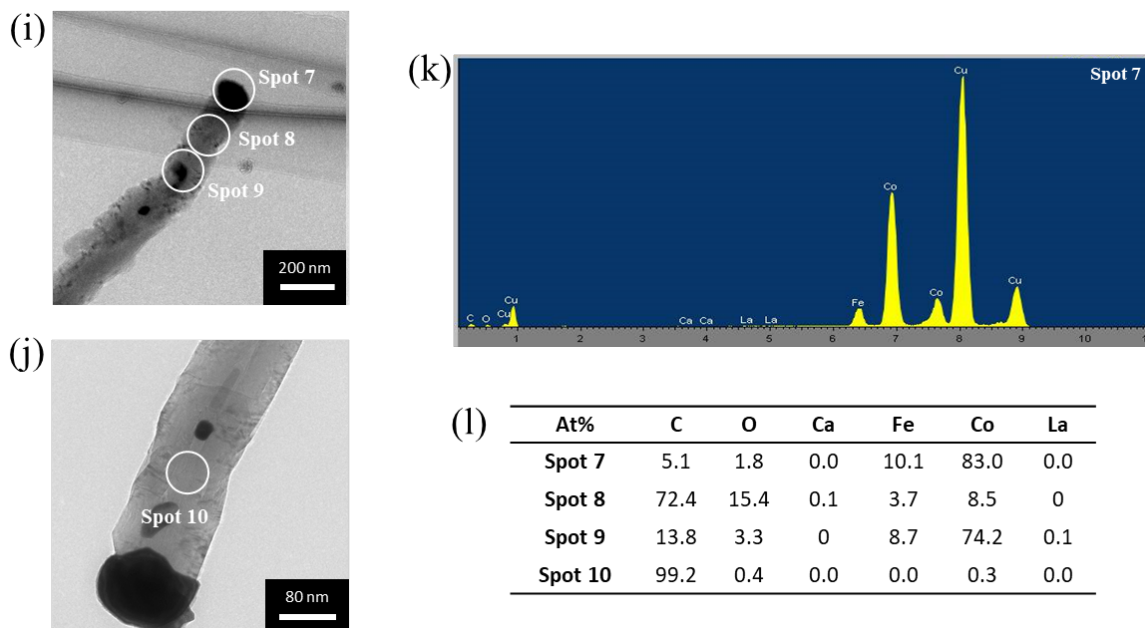
Figure 9. TEM images with EDXS spectra of the carbon materials produced using $La_{0.6}Ca_{0.4}Co_{1-x}Fe_xO_{3-\delta}$ (x = 0.2, 0.5, 0.8) pre-catalysts at a reaction temperature of 850 °C: (a,b,c,d) x = 0.2, (e,f,g,h) x = 0.5, and (i,j,k,l) x = 0.8. The element Cu is from the copper grid.

TPO analysis was also carried out to evaluate the quality and type of the carbon materials collected. For a better understanding and fair comparison, the TPO measurements were conducted for the fresh pre-catalysts as well. As observed from Figure 10 (a), there are no sharp and significant mass changes in the entire analyzed temperature range (up to 800 °C) for all the investigated pre-catalysts, which confirmed that the employed catalysts make only a neglectable contribution to the weight loss of the mixture of pre-catalysts and generated carbon materials. Oxidation of carbon materials caused the weight loss between 450 °C and 750 °C, and remaining weight was coming from the applied pre-catalysts. Among all the examined pre-catalysts, $La_{0.6}Ca_{0.4}Co_{0.2}Fe_{0.8}O_{3-\delta}$ demonstrated the greatest weight loss during TPO measurements at the reaction temperatures of 800 ℃ and 850 ℃, indicating the largest amount of carbon deposition on the surface. These TPO results accord well with the carbon deposition results shown in Figure 4. According to the literature, the peaks occurred in derivative weight profiles at around 520 °C~600 °C and 800 °C were standing for carbon nanotubes and carbon nanofibers, respectively [11,54,55]. As increasing the substitution content of Fe in the pre-catalysts, the derivative profiles showed that both oxidation peaks (see Figure 10) tended to shift to higher temperature for the three investigated reaction temperatures, which indicates the produced carbon materials possess a higher thermal stability. Moreover, the predominate

oxidation peaks are located at nearly 600 °C for the carbon materials generated with La$_{0.6}$Ca$_{0.4}$Co$_{0.2}$Fe$_{0.8}$O$_{3-\delta}$ at reaction temperatures of 800 °C and 850 °C, giving a hint to the resistance of the high crystallinity carbon materials.
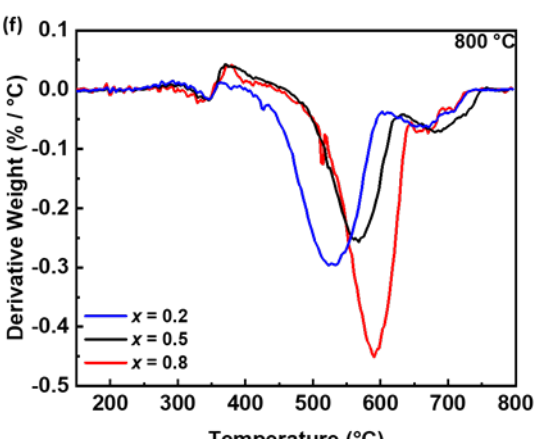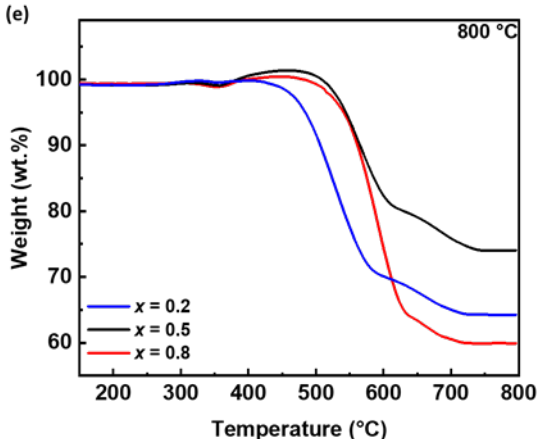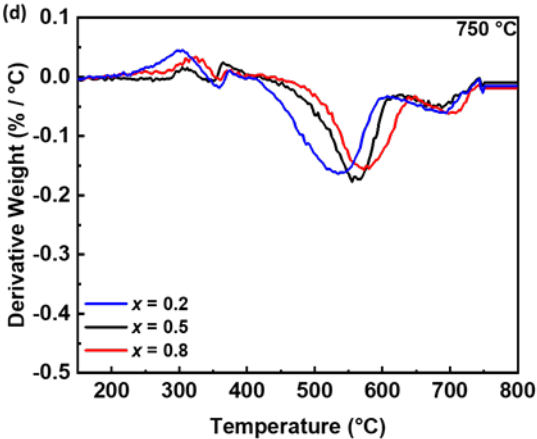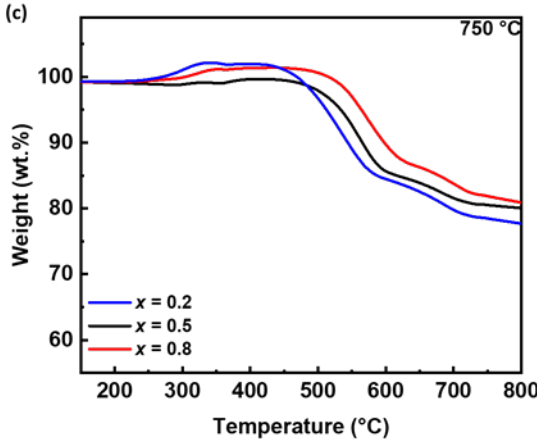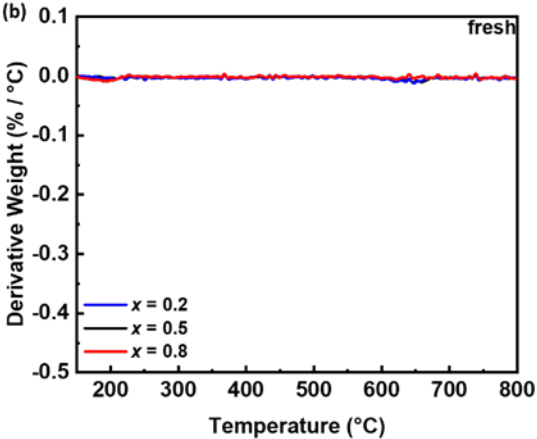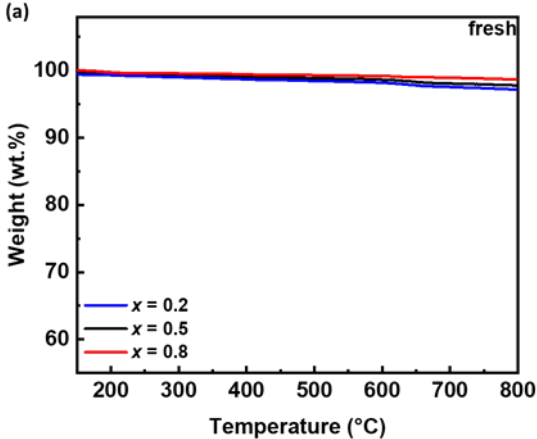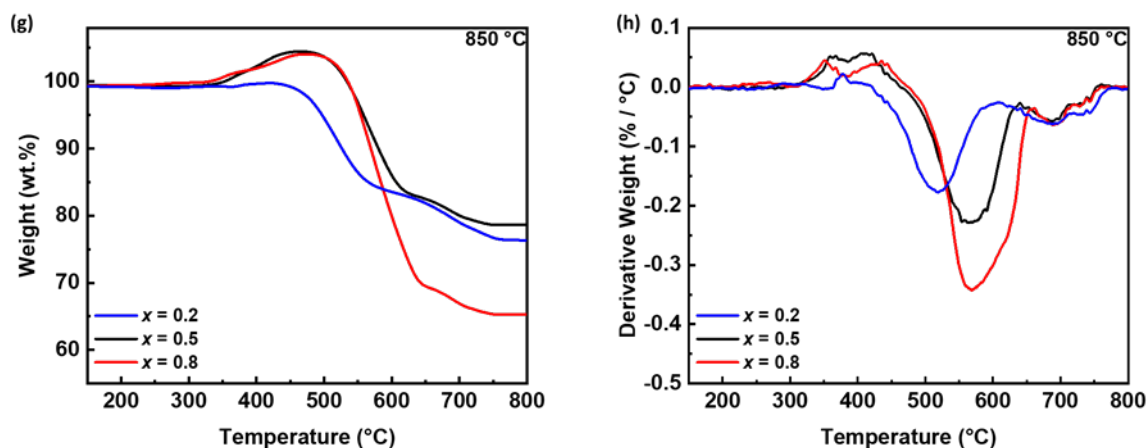
Figure 10. Temperature programmed oxidation (a, c, e, g) and derivative plots (b, d, f, h) of fresh pre-catalysts and carbon materials produced with $La_{0.6}Ca_{0.4}Co_{1-x}Fe_xO_{3-\delta}$ (x = 0.2, 0.5, 0.8) at different reaction temperatures.

Raman spectroscopy was also used to analyze the produced carbon materials in order to assess the purity and microstructural information of carbon nanotubes or nano filaments based on vibrational mode information. A Raman spectrum with three sharp bands can be identified from all the investigated samples as displayed in Figure 11. According to the reported literature, in graphene- and graphite-related carbons the D band at 1350 cm^{-1} is attributed to amorphous or disordered carbon and refers to a breathing mode of hexagonally arranged carbon atoms (A_{1g} symmetry) [56–60], whereas the G band at 1580 cm^{-1} is created by an in-plane mode (E_{2g} symmetry) of carbon atoms [57,58,60–62]. In single-walled carbon nanotubes (SWCNTs), the G band is a multiple peak due to curvature effects [63,64] and is related to the tangential modes [60,65]. The Raman characteristics of multi-walled carbon nanotubes (MWCNTs) might be attributed to the Raman characteristics of both SWCNTs and graphite-related carbons, their contributions to the spectra are not distinguishable [66]. When assuming MWCNTs consisting of many layers, the Raman features could be associated to similar processes like in graphite-related carbons, then similar vibrational mode and structure properties could be attained [60,67]. The G' band detected at roughly 2700 cm^{-1} links to the second-order two-phonon scattering process and an overtone of the D band [60,62,66,68]. The intensity ratio of the D and G band I_D/I_G is utilized to estimate the degree of disorder of the carbon deposits, and a higher ratio of $I_{G'}/I_G$ also indicates higher purity of carbon phase [11]. As shown in Figure 11, the produced carbon composites with different pre-catalysts at various catalysis temperatures have I_D/I_G ratios ranging from 0.34 to 0.97 and $I_{G'}/I_G$ ratios ranging from 0.35 to 0.63. For increasing reaction temperatures, a general trend to a lower I_D/I_G ratio can be observed, indicating a

decreasing degree of disorder [57]. At 800 °C, $La_{0.6}Ca_{0.4}Co_{0.2}Fe_{0.8}O_{3-\delta}$ showed an I_D/I_G ratio of 0.97. It might be caused by structural rearrangements as observed for other types of carbon [69], but would require further analysis. Interestingly, it was found that an increasing Fe/Co ratio in the $La_{0.6}Ca_{0.4}Co_{1-x}Fe_xO_{3-\delta}$ pre-catalysts promotes the formation of CNTs with higher carbonization degree and structural order at a reaction temperature of 850 °C. Among all the investigated pre-catalysts, the highest $I_{G'}/I_G$ of 0.63 and lowest I_D/I_G ratio of 0.34 were obtained with $La_{0.6}Ca_{0.4}Co_{0.2}Fe_{0.8}O_{3-\delta}$ pre-catalyst at 850 °C, which implies that the CNTs generated had higher graphite-like stacking order and fewer disorder.
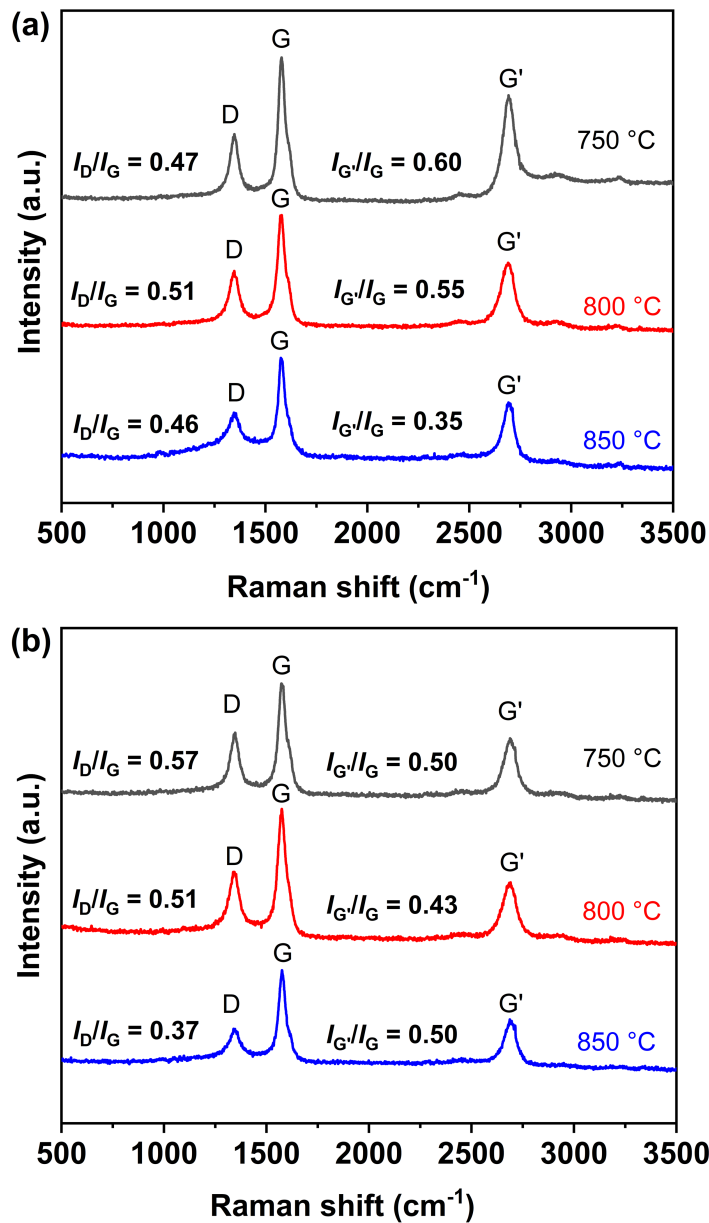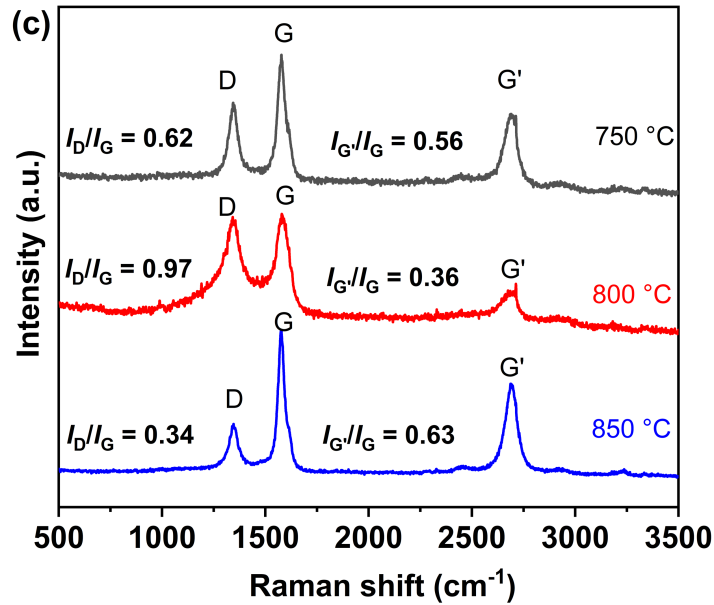
Figure 11. Raman analysis of carbon materials at different reaction temperatures over the $La_{0.6}Ca_{0.4}Co_{1-x}Fe_xO_{3-\delta}$ (x = 0.2, 0.5, 0.8) pre-catalysts at 532 nm laser excitation: (a) x = 0.2, (b) x = 0.5, and (c) x = 0.8.

3.4 Successive cycles of the thermal catalytic pyrolysis of used medical masks

Based on the above results, the $La_{0.6}Ca_{0.4}Co_{0.2}Fe_{0.8}O_{3-\delta}$ pre-catalyst demonstrated an excellent conversion performance especially at a reaction temperature of 850 °C towards hydrogen and high value-added carbon products comparing to the others. Therefore, further successive cycles of measurements were performed with this pre-catalyst to evaluate its deactivation behavior and potential to continue functioning during the thermal catalytic pyrolysis of plastics. 0.4 g pre-catalyst was employed throughout the experiment. Every cycle was performed directly following the previous cycle. Medical plastic wastes (0.4 g) were added sequentially with no further catalyst additions between each cycle. In order to maintain the same experimental conditions, the pre-catalysts were not collected after each cycle in this study. 10 successive cycles were performed. In general, the hydrogen yield from successive cycles of catalytic deconstruction of used medical masks fluctuated between 17.98 and 34.33 mmol / $g_{plastic}$. It can be observed from Figure 12(a), that the hydrogen yield reached 32.26 mmol / $g_{plastic}$ when fresh $La_{0.6}Ca_{0.4}Co_{0.2}Fe_{0.8}O_{3-\delta}$ was employed. The hydrogen yield then decreased in the following 5 cycles due to the accumulated carbon deposits, which was also observed in the reported studies [9,55]. Interestingly, the hydrogen yield reached its highest point of 34.33 mmol / $g_{plastic}$ at the 7th cycle. This enhanced hydrogen production could be linked to the catalytic destruction of hydrocarbon gases with the produced carbon materials (autocatalysis). Carbonaceous catalysts have been widely studied and proven to be effective catalysts for methane cracking for

hydrogen production with stable performances and high resistance to deactivation [70,71]. The decreased contents of hydrocarbon gases (CH_4 and C_2H_6) and increased content of H_2 in the gas composition as shown in Figure 12 (b) confirmed our hypothesis. Nevertheless, although the produced carbon materials can compensate the partial hindering of the active sites of the pre-catalysts, more and more catalytic active sites were still covered due to the large amount of accumulated carbon deposits over the entire cyclic measurements as shown in Figure 13, which led to the further decrease of hydrogen yield in the following cycles. This phenomenon becomes more apparent when four successive cycles of catalytic pyrolysis of used medical masks with a higher plastic/pre-catalyst ratio of 2.5 are performed (see Figure S7 and S8). Raman analysis was also performed on the spent catalysts after ten successive cycles of measurements and shown in Figure S9. Comparing with the single measurement, the produced carbon after 10 cycles holds a lower I_D/I_G ratio of 0.25, and a similar $I_{G'}/I_G$ ratio of 0.62. The generated metal oxide CNT composite materials in this work will be utilized directly in energy-storage materials without further separating process in future studies.

The H_2 yield and H_2 selectivity obtained in the present work from catalytic pyrolysis of plastic wastes are benchmarked with the representative literature studies as shown in Table 2. It can be shown that the values of H_2 yield and selectivity generated from our sequential experiments using the $La_{0.6}Ca_{0.4}Co_{0.2}Fe_{0.8}O_{3-\delta}$ pre-catalyst are among the highest observed for other approaches utilizing other catalysts. The presented results show that the perovskite-type $La_{0.6}Ca_{0.4}Co_{0.2}Fe_{0.8}O_{3-\delta}$ pre-catalyst with excellent performances and the potential to continue functioning make it a promising candidate for thermal catalytic decomposition of waste plastics for co-producing of hydrogen and carbon nanotube composites.
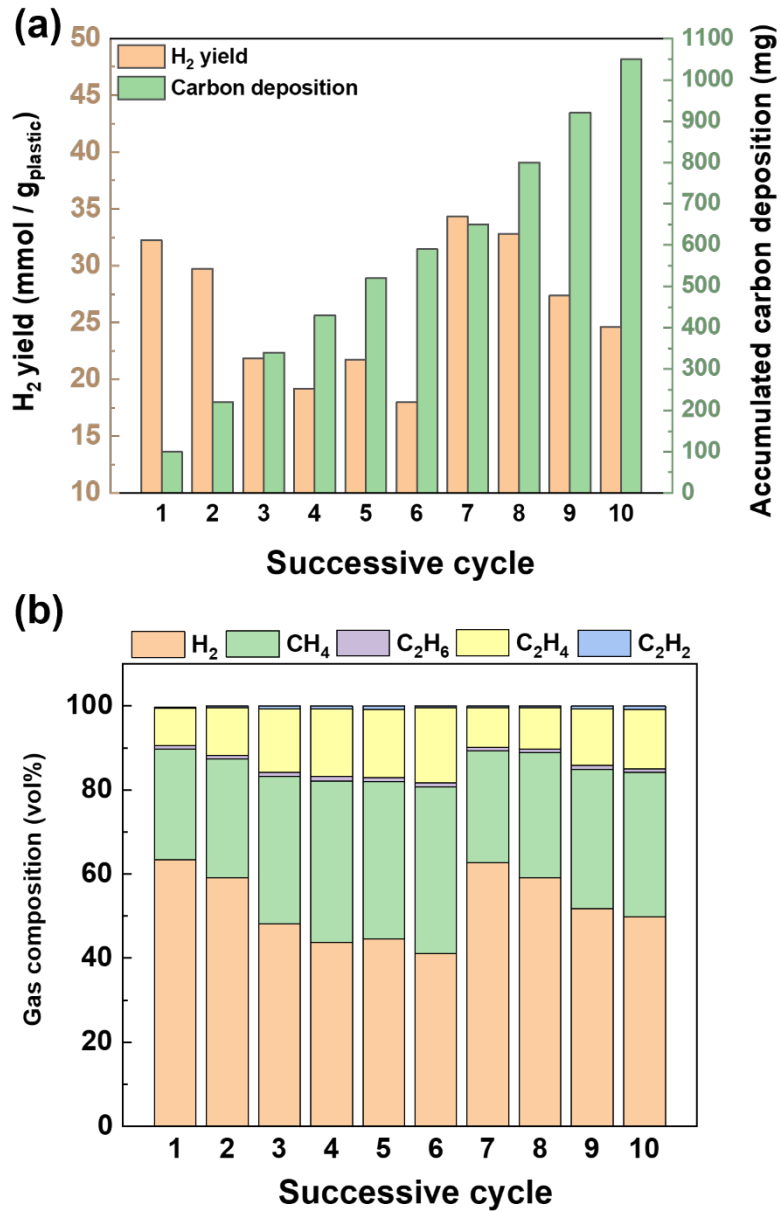
Figure 12. Successive cycles of the deconstruction of used medical masks over the La$_{0.6}$Ca$_{0.4}$Co$_{0.2}$Fe$_{0.8}$O$_{3-\delta}$ pre-catalyst at 850 ℃: (a) H$_2$ and solid (carbon) yields and (b) gas composition (vol%). 0.4 g of used medical masks is added to each cycle of measurement and the amount of pre-catalyst is 0.4 g.
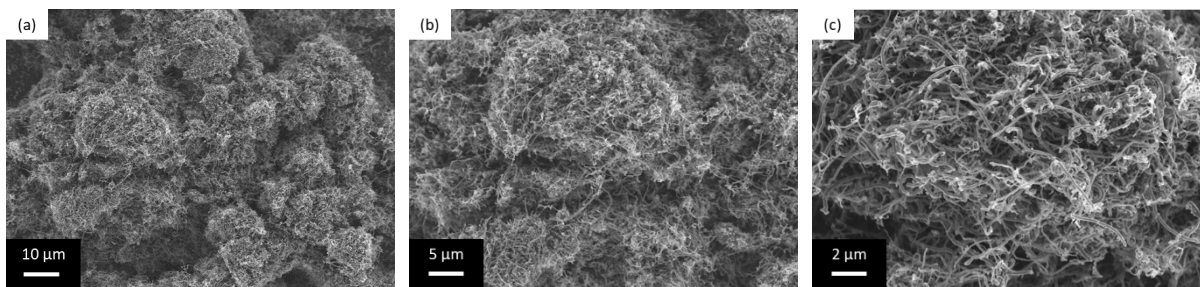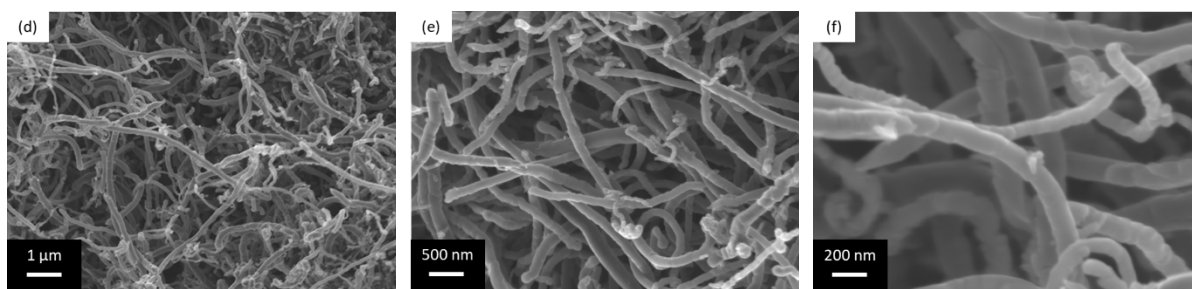
Figure 13. Low magnification (a,b,c) and high magnification (d,e,f) SEM images of spent $La_{0.6}Ca_{0.4}Co_{0.2}Fe_{0.8}O_{3-\delta}$ pre-catalyst at 850 °C after 10 successive cycles of the deconstruction of used medical masks.

Table 2 Summary of the products evolved from catalytic pyrolysis studies of plastic wastes.

Type of reactor	Catalyst	Type of plastic	Temperature (°C)	H_2 yield (mmol / $g_{plastic}$)	H_2 in the evolved gas (vol %)	Successive cycles			Ref.
						Cycle NO.	H_2 yield (mmol / $g_{plastic}$)	H_2 in the evolved gas (vol %)	
Two-stage fixed bed	$La_{0.6}Ca_{0.4}Co_{0.2}Fe_{0.8}O_{3-\delta}$	Used medical masks (PP)	850	34.3	62.7	10	24.6	49.9	This work
Microwave reactor	$FeAlO_x$	Real-world waste plastics (HDPE)	300-380	50.5	88.0	10	8.9	41.6	[55]
Two-stage fixed bed reactor	Ni(50)/C	Disposable face mask (PP)	800	21.5	49.9	-	-	-	[9]
	Zn/C		500	0.7	18.6	7	0.3	6.6	
Two-stage fixed bed reactor	FeNi1	PP	800	25.1	53.3	-	-	-	[36]
	FeNi2			20	46.7	-	-	-	
Two-stage fixed bed reactor	FeNi/Al	Landfill waste (mixture of PE; PP PS and PVC)	800	9.0 ± 0.2	50	-	-	-	[39]
			900	6.6 ±0.4	48	-	-	-	
Two-stage fixed bed reactor	$La_{0.8}Ni_{0.15}Fe_{0.85}O_{3-\delta}$	LDPE	800	24.5	74.8	-	-	-	[72]
		HDPE		23,2	72.58	-	-	-	
	$La_{0.8}Ni_{0.15}Co_{0.5}O_{3-\delta}$	PP	700	16.6	82.2	-	-	-	[41]

Reactor	Catalyst	Feedstock	Temperature						Ref.
Two-stage fixed bed reactor			800	19.8	-	-	-	-	-
			900	12.8	-	-	-	-	-
Two-stage fixed bed reactor	Ni/γ- Al$_2$O$_3$	Real-world waste plastics (mixture of HDPE; LDPE PP and PS)	800	22.5	52.6	-	-	-	[21]
	Fe/γ- Al$_2$O$_3$		800	22.9	57.5	-	-	-	
	Ni-Fe/γ-Al$_2$O$_3$			31.8	62.9	-	-	-	
	Ni-Fe/γ-Al$_2$O$_3$		900	43.7	72.2	-	-	-	
	Ni-Fe/γ-Al$_2$O$_3$		700	27.2	66.5	-	-	-	
Two-stage fixed bed reactor	Ni/ZSM5-30	HDPE	850	30.1	68.8	-	-	-	[73]
Two-stage fixed bed reactor	Fe-SiO$_2$-S	PP	800	15.4	41.7	-	-	-	[74]
	Fe-SiO$_2$-L			25.6	50.3	-	-	-	

4. Conclusions

This work studied the pyrolysis and catalytic decomposition pathway of medical waste plastics for a co-production of hydrogen and high value-added carbon nanomaterials by employing perovskite-type La$_{0.6}$Ca$_{0.4}$Co$_{1-x}$Fe$_x$O$_{3-\delta}$ pre-catalysts prepared via a scalable reverse co-precipitation approach. The experiments were carried out using a dual-stage fixed bed system and the effects of reaction temperature and pre-catalyst composition on the production of gas and carbon products were systematically investigated. The results reveal that the presence of the studied pre-catalysts considerably boosts the generation of both hydrogen and carbon nanomaterials. The higher Fe/Co ratio in the perovskite pre-catalysts resulted in a significant improvement of the hydrogen yield and promoted the formation of carbon nanotubes in the composites with a higher graphitic characteristics and purity based on the results by Raman spectral analysis. La$_{0.6}$Ca$_{0.4}$Co$_{0.2}$Fe$_{0.8}$O$_{3-\delta}$ pre-catalyst among all the investigated pre-catalysts produced the highest carbon nanotubes yield of 245 mg/g$_{plastic}$ and hydrogen yield of 24.92 mmol/g$_{plastic}$ at 850 °C, respectively. During the 10 cycles of successive decomposition of medical waste plastics, the pre-catalyst kept a high hydrogen yield of 24.63 mmol/g$_{plastic}$ after 10 cycles, with the highest hydrogen yield of 34.33 mmol/g$_{plastic}$ at the 7th cycle at 850 °C. The results show that the prepared perovskite-type La$_{0.6}$Ca$_{0.4}$Co$_{0.2}$Fe$_{0.8}$O$_{3-\delta}$ material is a promising pre-catalyst for thermal catalytic decomposition of medical waste plastics for producing hydrogen and carbon nanotube composites, e.g., for energy conversion and storage applications.

Acknowledgments

Authorship contribution statement

Xiao Yu: Conceptualization, Methodology, Validation, Writing – original draft. **Guoxing Chen**: Conceptualization, Supervision, Methodology, Validation, Writing – review & editing. **Marc Widenmeyer**: Methodology, Investigation, Validation, Writing – review & editing. **Isabel Kinski**: Validation, Writing – review & editing. **Xingmin Liu**: Writing – review & editing. **Ulrike Kunz**: Investigation, Writing – review & editing. **Dominique Schüpfer**: Writing – review & editing. **Leopoldo Molina-Luna**: Investigation, Writing – review & editing. **Xin Tu**: Methodology, Writing – review & editing. **Gert Homm**: Funding acquisition, Writing – review & editing. **Anke Weidenkaff**: Funding acquisition, Supervision, Writing – review & editing.

References

[1] X. Liu, T. Lei, A. Boré, Z. Lou, B. Abdouraman, W. Ma, Evolution of global plastic waste trade flows from 2000 to 2020 and its predicted trade sinks in 2030, J. Clean. Prod. 376 (2022) 134373. https://doi.org/10.1016/j.jclepro.2022.134373.

[2] R. Choudhary, A. Mukhija, S. Sharma, R. Choudhary, A. Chand, A.K. Dewangan, G.K. Gaurav, J.J. Klemeš, Energy-saving COVID-19 biomedical plastic waste treatment using the thermal - Catalytic pyrolysis, Energy (2022) 126096. https://doi.org/10.1016/j.energy.2022.126096.

[3] A.L. Patrício Silva, J.C. Prata, T.R. Walker, A.C. Duarte, W. Ouyang, D. Barcelò, T. Rocha-Santos, Increased plastic pollution due to COVID-19 pandemic: Challenges and recommendations, Chem. Eng. J. 405 (2021) 126683. https://doi.org/10.1016/j.cej.2020.126683.

[4] S. Ramalingam, R. Thamizhvel, S. Sudagar, R. Silambarasan, Production of third generation bio-fuel through thermal cracking process by utilizing Covid-19 plastic wastes, Mater. Today: Proc 72 (2023) 1618–1623. https://doi.org/10.1016/j.matpr.2022.09.430.

[5] Q. Wang, M. Zhang, R. Li, The COVID-19 pandemic reshapes the plastic pollution research - A comparative analysis of plastic pollution research before and during the pandemic, Environ. Res. 208 (2022) 112634. https://doi.org/10.1016/j.envres.2021.112634.

[6] J.P. Abraham, B.D. Plourde, L. Cheng, Using heat to kill SARS-CoV-2, Rev. Med. Virol. 30 (2020) e2115. https://doi.org/10.1002/rmv.2115.

[7] B. Debnath, S. Ghosh, N. Dutta, Resource Resurgence from COVID-19 Waste via Pyrolysis: a Circular Economy Approach, Circ. Econ. Sustain. 2 (2022) 211–220. https://doi.org/10.1007/s43615-021-00104-2.

[8] J. Wang, B. Shen, M. Lan, D. Kang, C. Wu, Carbon nanotubes (CNTs) production from catalytic pyrolysis of waste plastics: The influence of catalyst and reaction pressure, Catal. Today 351 (2020) 50–57. https://doi.org/10.1016/j.cattod.2019.01.058.

[9] Y. Jiang, R. Xu, C. Zeng, K. Wang, L. Han, X. Zhang, Scalable decomposition-catalysis of disposable COVID-19 face mask over self-assembly metal-doping carbocatalysts for tunable value-added products, Appl. Catal. B-Environ. 317 (2022) 121735. https://doi.org/10.1016/j.apcatb.2022.121735.

[10] C. Wang, R. Zou, H. Lei, M. Qian, X. Lin, W. Mateo, L. Wang, X. Zhang, R. Ruan, Biochar-advanced thermocatalytic salvaging of the waste disposable mask with the production of hydrogen and mono-aromatic hydrocarbons, J. Hazard. Mater. 426 (2022) 128080. https://doi.org/10.1016/j.jhazmat.2021.128080.

[11] Q. Cao, H.-C. Dai, J.-H. He, C.-L. Wang, C. Zhou, X.-F. Cheng, J.-M. Lu, Microwave-initiated MAX Ti3AlC2-catalyzed upcycling of polyolefin plastic wastes: Selective conversion to hydrogen and carbon nanofibers for sodium-ion battery, Appl. Catal. B Environ. 318 (2022) 121828. https://doi.org/10.1016/j.apcatb.2022.121828.

[12] X. Liu, W. Xie, M. Widenmeyer, H. Ding, G. Chen, D.M. de Carolis, K. Lakus-Wollny, L. Molina-Luna, R. Riedel, A. Weidenkaff, Upcycling Waste Plastics into Multi-Walled Carbon Nanotube Composites via $NiCo_2O_4$ Catalytic Pyrolysis, Catalysts 11 (2021) 1353. https://doi.org/10.3390/catal11111353.

[13] X. Liu, D. Xu, H. Ding, M. Widenmeyer, W. Xie, M. Mellin, F. Qu, G. Chen, Y.S. Zhang, Z. Zhang, A. Rashid, L. Molina-Luna, J.P. Hofmann, R. Riedel, D.J. Brett, A. Weidenkaff, Multi-scale designed $Co_xMn_{3-x}O_4$ spinels: Smart pre-catalysts towards high-efficiency pyrolysis-catalysis recycling of waste plastics, Appl. Catal. B Environ. 324 (2023) 122271. https://doi.org/10.1016/j.apcatb.2022.122271.

[14] G. Chen, X. Tu, G. Homm, A. Weidenkaff, Plasma pyrolysis for a sustainable hydrogen economy, Nat Rev Mater 7 (2022) 333–334. https://doi.org/10.1038/s41578-022-00439-8.

[15] M. Markiewicz, Y.Q. Zhang, A. Bösmann, N. Brückner, J. Thöming, P. Wasserscheid, S. Stolte, Environmental and health impact assessment of Liquid Organic Hydrogen Carrier (LOHC) systems – challenges and preliminary results, Energy Environ. Sci. 8 (2015) 1035–1045. https://doi.org/10.1039/C4EE03528C.

[16] J. Yang, A. Sudik, C. Wolverton, D.J. Siegel, High capacity hydrogen storage materials: attributes for automotive applications and techniques for materials discovery, Chem. Soc. Rev. 39 (2010) 656–675. https://doi.org/10.1039/b802882f.

[17] L. Schlapbach, A. Züttel, Hydrogen-storage materials for mobile applications, Nature 414 (2001) 353–358. https://doi.org/10.1038/35104634.

[18] U. Eberle, B. Müller, R. von Helmolt, Fuel cell electric vehicles and hydrogen infrastructure: status 2012, Energy Environ. Sci. 5 (2012) 8780. https://doi.org/10.1039/c2ee22596d.

[19] K.A. Graves, L.J. Higgins, M.A. Nahil, B. Mishra, P.T. Williams, Structural comparison of multi-walled carbon nanotubes produced from polypropylene and polystyrene waste plastics, J. Anal. Appl. Pyrolysis 161 (2022) 105396. https://doi.org/10.1016/j.jaap.2021.105396.

[20] J.C. Acomb, C. Wu, P.T. Williams, Effect of growth temperature and feedstock:catalyst ratio on the production of carbon nanotubes and hydrogen from the pyrolysis of waste plastics, J. Anal. Appl. Pyrolysis 113 (2015) 231–238. https://doi.org/10.1016/j.jaap.2015.01.012.

[21] D. Yao, Y. Zhang, P.T. Williams, H. Yang, H. Chen, Co-production of hydrogen and carbon nanotubes from real-world waste plastics: Influence of catalyst composition and operational parameters, Appl. Catal. B Environ. 221 (2018) 584–597. https://doi.org/10.1016/j.apcatb.2017.09.035.

[22] A. Dupuis, The catalyst in the CCVD of carbon nanotubes—a review, Prog. Mater. Sci. 50 (2005) 929–961. https://doi.org/10.1016/j.pmatsci.2005.04.003.

[23] S. Kumar, M. Nehra, D. Kedia, N. Dilbaghi, K. Tankeshwar, K.-H. Kim, Carbon nanotubes: A potential material for energy conversion and storage, Prog. Energy and Combust. Sci. 64 (2018) 219–253. https://doi.org/10.1016/j.pecs.2017.10.005.

[24] F. Pyatkov, V. Fütterling, S. Khasminskaya, B.S. Flavel, F. Hennrich, M.M. Kappes, R. Krupke, W.H.P. Pernice, Cavity-enhanced light emission from electrically driven carbon nanotubes, Nat. Photon 10 (2016) 420–427. https://doi.org/10.1038/nphoton.2016.70.

[25] L. Wen, F. Li, H.-M. Cheng, Carbon Nanotubes and Graphene for Flexible Electrochemical Energy Storage: from Materials to Devices, Adv. Mater. 28 (2016) 4306–4337. https://doi.org/10.1002/adma.201504225.

[26] M.F.L. de Volder, S.H. Tawfick, R.H. Baughman, A.J. Hart, Carbon nanotubes: present and future commercial applications, Science 339 (2013) 535–539. https://doi.org/10.1126/science.1222453.

[27] S.H. Gebre, M.G. Sendeku, M. Bahri, Recent Trends in the Pyrolysis of Non-Degradable Waste Plastics, ChemistryOpen 10 (2021) 1202–1226. https://doi.org/10.1002/open.202100184.

[28] A. Fivga, I. Dimitriou, Pyrolysis of plastic waste for production of heavy fuel substitute: A techno-economic assessment, Energy 149 (2018) 865–874. https://doi.org/10.1016/j.energy.2018.02.094.

[29] E.O. Osung, S.B. Alabi, Techno-Economic Evaluation of Thermal and Catalytic Pyrolysis Plants for the Conversion of Heterogeneous Waste Plastics to Liquid Fuels in Nigeria, JPEE 10 (2022) 56–69. https://doi.org/10.4236/jpee.2022.107004.

[30] N. Cai, X. Li, S. Xia, L. Sun, J. Hu, P. Bartocci, F. Fantozzi, P.T. Williams, H. Yang, H. Chen, Pyrolysis-catalysis of different waste plastics over Fe/Al_2O_3 catalyst: High-value hydrogen, liquid fuels, carbon nanotubes and possible reaction mechanisms, Energy Convers. Manag. 229 (2021) 113794. https://doi.org/10.1016/j.enconman.2020.113794.

[31] D. Yao, C.-H. Wang, Pyrolysis and in-line catalytic decomposition of polypropylene to carbon nanomaterials and hydrogen over Fe- and Ni-based catalysts, Appl. Energy 265 (2020) 114819. https://doi.org/10.1016/j.apenergy.2020.114819.

[32] A. Ochoa, I. Barbarias, M. Artetxe, A.G. Gayubo, M. Olazar, J. Bilbao, P. Castaño, Deactivation dynamics of a Ni supported catalyst during the steam reforming of volatiles from waste polyethylene pyrolysis, Appl. Catal. B Environ. 209 (2017) 554–565. https://doi.org/10.1016/j.apcatb.2017.02.015.

[33] L. Garcia, R. French, S. Czernik, E. Chornet, Catalytic steam reforming of bio-oils for the production of hydrogen: effects of catalyst composition, Appl. Catal. A-Gen. 201 (2000) 225–239. https://doi.org/10.1016/S0926-860X(00)00440-3.

[34] H. Ago, N. Uehara, N. Yoshihara, M. Tsuji, M. Yumura, N. Tomonaga, T. Setoguchi, Gas analysis of the CVD process for high yield growth of carbon nanotubes over metal-supported catalysts, Carbon 44 (2006) 2912–2918. https://doi.org/10.1016/j.carbon.2006.05.049.

[35] S.-M. Tan, S.-P. Chai, W.-W. Liu, A.R. Mohamed, Effects of FeO_x, CoO_x, and NiO catalysts and calcination temperatures on the synthesis of single-walled carbon nanotubes through chemical vapor deposition of methane, J. Alloys Compd. 477 (2009) 785–788. https://doi.org/10.1016/j.jallcom.2008.10.114.

[36] D. Yao, H. Li, Y. Dai, C.-H. Wang, Impact of temperature on the activity of Fe-Ni catalysts for pyrolysis and decomposition processing of plastic waste, Chem Eng. J. 408 (2021) 127268. https://doi.org/10.1016/j.cej.2020.127268.

[37] T. Maneerung, K. Hidajat, S. Kawi, Co-production of hydrogen and carbon nanofibers from catalytic decomposition of methane over $LaNi_{(1-x)}M_x O_{3-\alpha}$ perovskite (where M = Co, Fe and X = 0, 0.2, 0.5, 0.8, 1), Int. J. Hydrog. Energy 40 (2015) 13399–13411. https://doi.org/10.1016/j.ijhydene.2015.08.045.

[38] J. Zhu, H. Li, L. Zhong, P. Xiao, X. Xu, X. Yang, Z. Zhao, J. Li, Perovskite Oxides: Preparation, Characterizations, and Applications in Heterogeneous Catalysis, ACS Catal. 4 (2014) 2917–2940. https://doi.org/10.1021/cs500606g.

[39] K. Jagodzińska, P.G. Jönsson, W. Yang, Pyrolysis and in-line catalytic decomposition of excavated landfill waste to produce carbon nanotubes and hydrogen over Fe- and Ni-based catalysts – Investigation of the catalyst type and process temperature, Chem. Eng. J. 446 (2022) 136808. https://doi.org/10.1016/j.cej.2022.136808.

[40] J. Liu, Z. Jiang, H. Yu, T. Tang, Catalytic pyrolysis of polypropylene to synthesize carbon nanotubes and hydrogen through a two-stage process, Polym. Degrad. Stab. 96 (2011) 1711–1719. https://doi.org/10.1016/j.polymdegradstab.2011.08.008.

[41] J. Jia, A. Veksha, T.-T. Lim, G. Lisak, Temperature-dependent synthesis of multi-walled carbon nanotubes and hydrogen from plastic waste over A-site-deficient perovskite $La_{0.8}Ni_{1-x}Co_xO_{3-\delta}$, Chemosphere 291 (2022) 132831. https://doi.org/10.1016/j.chemosphere.2021.132831.

[42] Z. Wang, L. Zou, S. Guo, M. Sun, Y. Chen, B. Chi, J. Pu, J. Li, Porous double-doped perovskite $La_{0.6}Ca_{0.4}Fe_{0.8}Ni_{0.2}O_3$ nanotubes as highly efficient bifunctional catalysts for lithium-oxygen batteries, J. Power Sources 468 (2020) 228362. https://doi.org/10.1016/j.jpowsour.2020.228362.

[43] A. Weidenkaff, S.G. Ebbinghaus, T. Lippert, $Ln_{1-x}A_xCoO_3$ (Ln = Er, La; A = Ca, Sr)/Carbon Nanotube Composite Materials Applied for Rechargeable Zn/Air Batteries, Chem. Mater. 14 (2002) 1797–1805. https://doi.org/10.1021/cm011305v.

[44] M.J. Montenegro, M. Döbeli, T. Lippert, S. Müller, B. Schnyder, A. Weidenkaff, P.R. Willmott, A. Wokaun, Pulsed laser deposition of $La_{0.6}Ca_{0.4}CoO_3$ (LCCO) films. A promising metal-oxide catalyst for air based batteries, Phys. Chem. Chem. Phys. 4 (2002) 2799–2805. https://doi.org/10.1039/b200120a.

[45] D.-M. Amaya-Dueñas, G. Chen, A. Weidenkaff, N. Sata, F. Han, I. Biswas, R. Costa, K.A. Friedrich, A -site deficient chromite with in situ Ni exsolution as a fuel electrode for solid oxide cells (SOCs), J. Mater. Chem. A 9 (2021) 5685–5701. https://doi.org/10.1039/D0TA07090D.

[46] G. Chen, W. Liu, M. Widenmeyer, P. Ying, M. Dou, W. Xie, C. Bubeck, L. Wang, M. Fyta, A. Feldhoff, A. Weidenkaff, High flux and CO_2-resistance of $La_{0.6}Ca_{0.4}Co_{1-x}Fe_xO_{3-\delta}$ oxygen-transporting membranes, J. Membr. Sci. 590 (2019) 117082. https://doi.org/10.1016/j.memsci.2019.05.007.

[47] N.A. Merino, B.P. Barbero, C. Cellier, J.A. Gamboa, L.E. Cadús, Effect of the calcium on the textural, structural and catalytic properties of $La_{1-x}Ca_xCo_{1-y}Fe_yO_3$ perovskites, Catal. Lett. 113 (2007) 130–140. https://doi.org/10.1007/s10562-007-9017-9.

[48] R.D. Shannon, Revised effective ionic radii and systematic studies of interatomic distances in halides and chalcogenides, Acta Crystallogr. 32 (1976) 751–767. https://doi.org/10.1107/S0567739476001551.

[49] S. Prabu, K.-Y. Chiang, Highly active Ni–Mg–Al catalyst effect on carbon nanotube production from waste biodegradable plastic catalytic pyrolysis, Enviro. Technol. Innov. 28 (2022) 102845. https://doi.org/10.1016/j.eti.2022.102845.

[50] W.-W. Liu, A. Aziz, S.-P. Chai, A.R. Mohamed, U. Hashim, Synthesis of Single-Walled Carbon Nanotubes: Effects of Active Metals, Catalyst Supports, and Metal Loading Percentage, J. Nanomater. 2013 (2013) 1–8. https://doi.org/10.1155/2013/592464.

[51] D. Yao, C. Wu, H. Yang, Y. Zhang, M.A. Nahil, Y. Chen, P.T. Williams, H. Chen, Co-production of hydrogen and carbon nanotubes from catalytic pyrolysis of waste plastics on Ni-Fe bimetallic

catalyst, Energy Convers. Manag. 148 (2017) 692–700. https://doi.org/10.1016/j.enconman.2017.06.012.

[52] J.C. Acomb, C. Wu, P.T. Williams, The use of different metal catalysts for the simultaneous production of carbon nanotubes and hydrogen from pyrolysis of plastic feedstocks, Appl. Catal. B Environ. 180 (2016) 497–510. https://doi.org/10.1016/j.apcatb.2015.06.054.

[53] G. Du, S. Feng, J. Zhao, C. Song, S. Bai, Z. Zhu, Particle-wire-tube mechanism for carbon nanotube evolution, J. Am. Chem. Soc. 128 (2006) 15405–15414. https://doi.org/10.1021/ja064151z.

[54] D. Xu, Y. Xiong, J. Ye, Y. Su, Q. Dong, S. Zhang, Performances of syngas production and deposited coke regulation during co-gasification of biomass and plastic wastes over $Ni/\gamma-Al_2O_3$ catalyst: Role of biomass to plastic ratio in feedstock, Chem. Eng. J. 392 (2020) 123728. https://doi.org/10.1016/j.cej.2019.123728.

[55] X. Jie, W. Li, D. Slocombe, Y. Gao, I. Banerjee, S. Gonzalez-Cortes, B. Yao, H. AlMegren, S. Alshihri, J. Dilworth, J. Thomas, T. Xiao, P. Edwards, Microwave-initiated catalytic deconstruction of plastic waste into hydrogen and high-value carbons, Nat. Catal. 3 (2020) 902–912. https://doi.org/10.1038/s41929-020-00518-5.

[56] F. Tuinstra, J.L. Koenig, Raman Spectrum of Graphite, J. Chem. Phys. 53 (1970) 1126–1130. https://doi.org/10.1063/1.1674108.

[57] A.C. Ferrari, J. Robertson, Interpretation of Raman spectra of disordered and amorphous carbon, Phys. Rev. B 61 (2000) 14095–14107. https://doi.org/10.1103/PhysRevB.61.14095.

[58] A.C. Ferrari, D.M. Basko, Raman spectroscopy as a versatile tool for studying the properties of graphene, Nat. Nanotechnol. 8 (2013) 235–246. https://doi.org/10.1038/nnano.2013.46.

[59] S.D.M. Brown, A. Jorio, M.S. Dresselhaus, G. Dresselhaus, Observations of the D -band feature in the Raman spectra of carbon nanotubes, Phys. Rev. B 64 (2001). https://doi.org/10.1103/PhysRevB.64.073403.

[60] A. Jorio, Raman spectroscopy in graphene related systems, Wiley-VCH, Weinheim, 2013.

[61] R. Vidano, D.B. Fischbach, New Lines in the Raman Spectra of Carbons and Graphite, J. Am. Ceram. Soc. 61 (1978) 13–17. https://doi.org/10.1111/j.1151-2916.1978.tb09219.x.

[62] L.M. Malard, M.A. Pimenta, G. Dresselhaus, M.S. Dresselhaus, Raman spectroscopy in graphene, Phys. Rep. 473 (2009) 51–87. https://doi.org/10.1016/j.physrep.2009.02.003.

[63] M.S. Dresselhaus, P.C. Eklund, Phonons in carbon nanotubes, Adv. Phys. 49 (2000) 705–814. https://doi.org/10.1080/000187300413184.

[64] M.S. Dresselhaus, G. Dresselhaus, A. Jorio, A.G. Souza Filho, R. Saito, Raman spectroscopy on isolated single wall carbon nanotubes, Carbon 40 (2002) 2043–2061. https://doi.org/10.1016/S0008-6223(02)00066-0.

[65] J.M. Holden, P. Zhou, X.-X. Bi, P.C. Eklund, S. Bandow, R.A. Jishi, K. Das Chowdhury, G. Dresselhaus, M.S. Dresselhaus, Raman scattering from nanoscale carbons generated in a cobalt-

catalyzed carbon plasma, Chem. Phys. Lett. 220 (1994) 186–191. https://doi.org/10.1016/0009-2614(94)00154-5.

[66] M.S. Dresselhaus, G. Dresselhaus, R. Saito, A. Jorio, Raman spectroscopy of carbon nanotubes, Phys. Rep. 409 (2005) 47–99. https://doi.org/10.1016/j.physrep.2004.10.006.

[67] P. Tan, L. An, L. Liu, Z. Guo, R. Czerw, D.L. Carroll, P.M. Ajayan, N. Zhang, H. Guo, Probing the phonon dispersion relations of graphite from the double-resonance process of Stokes and anti-Stokes Raman scatterings in multiwalled carbon nanotubes, Phys. Rev. B 66 (2002) 245410. https://doi.org/10.1103/PhysRevB.66.245410.

[68] R.J. Nemanich, S.A. Solin, First- and second-order Raman scattering from finite-size crystals of graphite, Phys. Rev. B 20 (1979) 392–401. https://doi.org/10.1103/PhysRevB.20.392.

[69] D.B. Schuepfer, F. Badaczewski, J.M. Guerra-Castro, D.M. Hofmann, C. Heiliger, B. Smarsly, P.J. Klar, Assessing the structural properties of graphitic and non-graphitic carbons by Raman spectroscopy, Carbon 161 (2020) 359–372. https://doi.org/10.1016/j.carbon.2019.12.094.

[70] M. Msheik, S. Rodat, S. Abanades, Methane Cracking for Hydrogen Production: A Review of Catalytic and Molten Media Pyrolysis, Energies 14 (2021) 3107. https://doi.org/10.3390/en14113107.

[71] M. Yousefi, S. Donne, Technical challenges for developing thermal methane cracking in small or medium scales to produce pure hydrogen - A review, Int. J. Hydro. Energy 47 (2022) 699–727. https://doi.org/10.1016/j.ijhydene.2021.10.100.

[72] J. Jia, A. Veksha, T.-T. Lim, G. Lisak, Weakening the strong Fe-La interaction in A-site-deficient perovskite via Ni substitution to promote the thermocatalytic synthesis of carbon nanotubes from plastics, J. Hazard. Mater. 403 (2021) 123642. https://doi.org/10.1016/j.jhazmat.2020.123642.

[73] D. Yao, H. Yang, H. Chen, P.T. Williams, Investigation of nickel-impregnated zeolite catalysts for hydrogen/syngas production from the catalytic reforming of waste polyethylene, Appl. Catal. B Environ. 227 (2018) 477–487. https://doi.org/10.1016/j.apcatb.2018.01.050.

[74] X. Liu, Y. Zhang, M.A. Nahil, P.T. Williams, C. Wu, Development of Ni- and Fe- based catalysts with different metal particle sizes for the production of carbon nanotubes and hydrogen from thermo-chemical conversion of waste plastics, J. Anal. Appl. Pyrolysis 125 (2017) 32–39. https://doi.org/10.1016/j.jaap.2017.05.001.